Electrocatalytic Effects of (Zr, Ti, Mo)-Doped Niobium Pentoxide Nanocrystal Impregnated Carbon Felt for Vanadium Redox Flow Batteries

Keith Steele

A dissertation

submitted in partial fulfillment of the

requirements for the degree of

Master of Science

University of Washington

2018

Committee:

Guozhong Cao, Chair

Lucien Brush

Program Authorized to Offer Degree:

Materials Science and Engineering

University of Washington

Abstract

Electrocatalytic Effects of (Zr, Ti, Mo)-Doped Niobium Pentoxide Nanocrystal Impregnated Carbon Felt for Vanadium Redox Flow Batteries

Keith Steele

Chair of the Supervisory Committee:
Dr. Guozhong Cao
Materials Science and Engineering

The electrocatalytic effectiveness of titanium, molybdenum, and as zirconium dopants added to (10 w/o W)-Nb2O5 impregnated carbon felt is investigated as possible improvements to carbon felt electrodes for use in vanadium redox flow batteries. Because the presence of dopants affects both the electrical and morphological properties of the oxides, the electrochemical kinetics cannot be separated neatly from the surface area of the tested samples. To compare these compositions, the Electroactive Area parameter is introduced as a combination of electrode surface area and an overall kinetics function. Additional measurements are made to quantify the relative amounts of deposited mass, diffraction patterns of the oxide-impregnated carbon felt, electrical parameters of the equivalent circuit via EIS, and the total surface area by gas sorption analysis and BET theory.

TABLE OF CONTENTS

LIST OF FIGURES

LIST OF TABLES

ACKNOWLEDGEMENTS

The author would like to thank Dr. Guozhong Cao for advice and guidance in performing this research, and the Materials Science and Engineering department for generosity with department assets.

Chapter 1. INTRODUCTION

The vanadium redox flow battery (VRFB), originally proposed by the Skyllas-Kazacos research group at the University of New South Wales[1,2] shows great promise as a developing energy storage technology. Recent reviews on the subject of VRFBs focus on advances in cost reduction of energy storage (measured in $/kWh), and the US Department of Energy has set a target cost of $100/kWh to allow the technology to achieve widespread market adoption.[3]

The design of the VRFB uses two electrolytes, each containing a different redox couple between two different oxidation states of vanadium. In the positive electrolyte ("catholyte"), the half-reaction is

$$VO^{2+} + e^- + 2H^+ \leftrightarrow VO^{2+} + H_2O \ (E^0 = 1.00\ V\ vs.SHE) \textbf{ (1)}$$

In the negative electrolyte ("anolyte"), the half-reaction is

$$V^{3+} + e^- \leftrightarrow V^{2+} \ (E^0 = 0.255\ V\ vs.SHE) \textbf{ (2)}$$

The complex nature of the catholyte reaction and large number of chemical participants leads to slow kinetics, which can limit the rate at which a VRFB can be charged and discharged. A commonly accepted reaction mechanism had three steps, and is dependent upon the surface oxygen atoms of the electrode.[4]

A VRFB cell contains the two electrolytes separated by a semipermeable membrane. External to the cell, two tanks hold extra electrolyte which is pumped through the cell. The state of charge is equivalent to the concentrations of the oxidation states of vanadium in each electrolyte: a fully charged battery has all V(II) in the anolyte and all V(V) in the catholyte, and a fully discharged battery has all V(III) in the anolyte and all V(IV) in the catholyte.

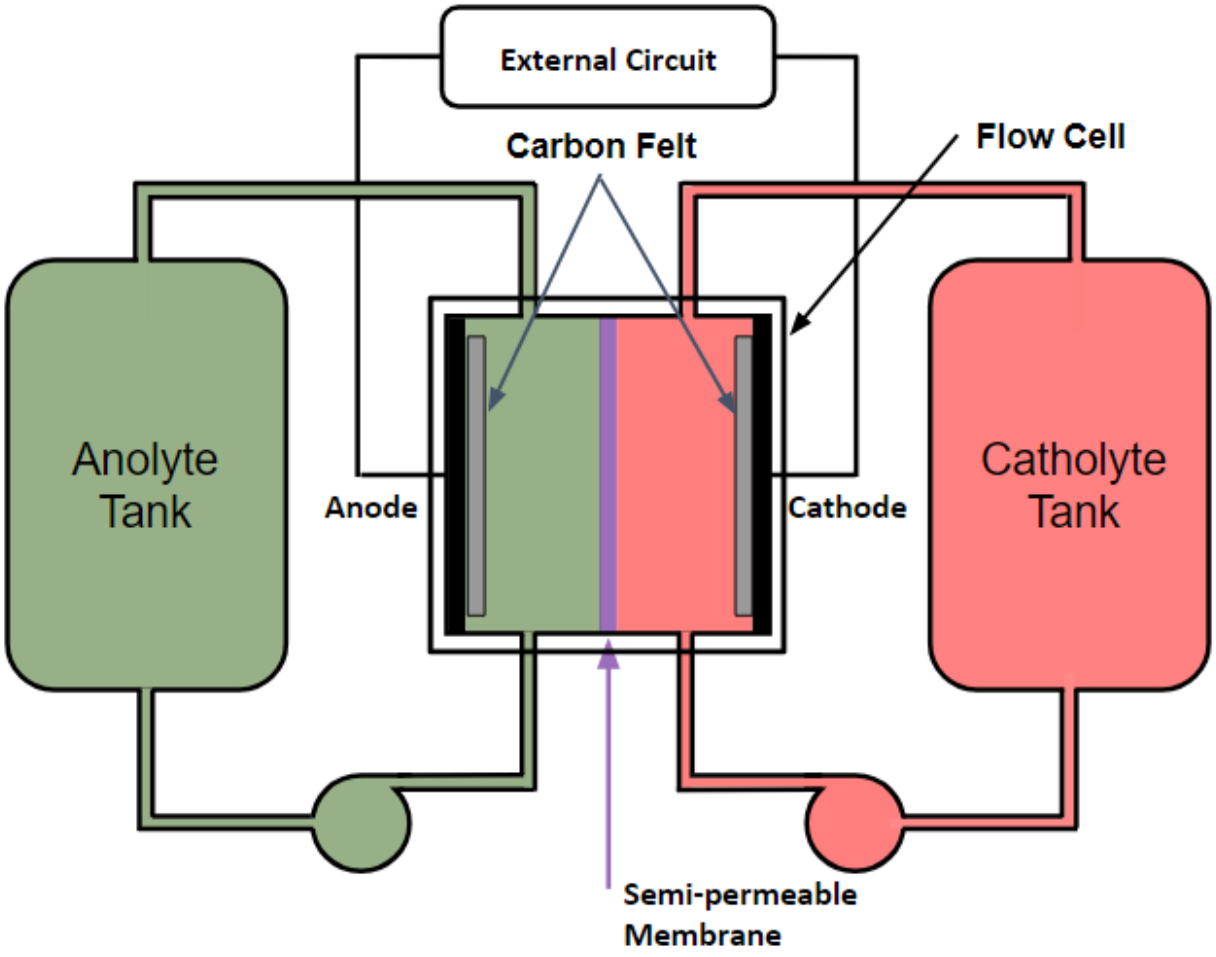

Fig. 1.1 Basic design of a VRFB

This battery design offers some unique advantages over the more widespread lithium-ion and lead-acid battery designs. The electrodes catalyze but do not participate in the redox reactions, and in an ideal battery the only component that degrades over time is the electrolyte, which can be replaced quickly by pumping in replacement electrolyte. The used electrolyte can be fully recovered into a useful form as long as it is not contaminated by foreign matter or other metal species.

The power and energy capacities of a VRFB are separately scaleable, and scaling a battery up or down for either parameter can be done by modular adjustment to a battery without disassembling it. Increasing or decreasing the energy capacity is achieved by increasing or decreasing the amount of electrolyte available to the system, by adding or subtracting tank volume. The power capacity can be increased by adding more cells to the system connected to the same pumps and electrolyte tanks. This allows for more versatile applications than lithium-ion and lead-acid batteries, because scaling those battery designs up or down must be done for power and energy capacities simultaneously.

The electrolyte limits the energy and power densities due to the solubility limit of vanadium ions in aqueous solution. To prevent precipitation of vanadium ions in an electrolyte of acidic solution with 2 M vanadium in different oxidation states, the typical operating temperature limits for a VRFB are set to 10-40 °C.[5] The self-discharge process of the VRFB requires crossover of vanadium ions from one electrolyte to the other, by diffusion and/or migration across the semi-permeable membrane. Other redox flow battery chemistries exist, such as vanadium-bromine, manganese-vanadium, and vanadium-cerium[5], as well as non-metallic chemistries like hydroquinone-bromine[6]. The advantage of the all-vanadium RFB is that ionic crossover reduces capacity but does not contaminate the electrolytes. While the rate of self-discharge of VRFBs is low compared to other battery designs, more selective membranes could improve this efficiency further.

Improving the kinetics of the catholyte reaction is the ultimate goal of this project. Several methods have been demonstrated, including increasing the carbon felt surface area by bonding porous carbon derived from organic sol-gel methods[7] or from plant sources[8], doping the carbon felt by the use of oxygen and nitrogen plasma,[9] and impregnating the surface of carbon

felt with electrocatalytic metals and metal oxides, including bismuth[10], copper[11], and Nb_2O_5[12]. This last method has the potential to be improved by the addition of small amounts of other metals, as discussed below, and the present work seeks to investigate the effectiveness of such doped metal oxide nanostructures on carbon felt.

Niobium pentoxide is an intrinsic n-type semiconductor with a wide bandgap energy of around 3.4 eV[13], and it exhibits poor conduction properties in its pure state. This current resistance may hinder its ability to transfer charge between a redox reaction happening at the electrode surface and the carbon felt substrate, reducing its catalytic effect. The introduction of a tetravalent transition metal M (which may be zirconium or titanium) is expected to increase the number of electron-donor defects and oxygen vacancies in the solid, expressed in the following reaction:

$$2MO_2(s) + 2V_{Nb}''''' + 5V_O^{\cdot\cdot} \rightarrow 2M_{Nb}' + 4O_O^x + V_O^{\cdot\cdot}$$

This mechanism of increasing conductivity is consistent with previous work measuring rapid changes in Nb2O5 conductivity with increases in the number of oxygen vacancies.[14]

Following Li et al.[12], the niobium pentoxide nanoparticles are synthesized with a tungsten precursor additive. The purpose and electroactive effect of tungsten is explored by synthesizing doped or undoped niobium pentoxide nanoparticles with and without this tungsten component, and by replacing it with molybdenum, another hexavalent metal.

Because the carbon felt material is composed of many small (~10 micrometer diameter) carbon fibers, its physical geometry is extremely complex and it has very high specific surface area. This geometry is further complicated by the mechanical contact of the fibers and by the surface roughness caused by thermal activation, and by nanoparticle impregnation. No quantitative method to measure the carbon felt surface coverage of nanoparticles could be

employed; instead, the effective surface area per mass of material for each sample under consideration was measured electrochemically. Qualitative verification of nanoparticle coverage of the carbon fibers was accomplished by taking SEM images.

The measurement of electrode surface area and the electrochemical kinetics of the electrode material are not separately measurable by electrochemical means, except in special circumstances.[15] Methods involving simplification of the electrode area have been employed, such as mixing carbon and oxide materials into an ink solution, painting this solution onto a glassy carbon electrode, and coating the electrode with a barrier substance such as Nafion.[12] However, the desired measurement should account for changes in diffusion in the bulk of the carbon felt, as well as other surface effects which are not necessarily conserved. For this reason, carbon felt samples were tested in their as-synthesized form, the same form which would be used in a flow battery. The drawback to this method is that the electrode area is unknown; therefore, the method of this experiment measures an "electroactive area", a term which has the units of area, but is modified by a scalar term to take the reaction kinetics into account.

For a reversible reaction governed by semi-infinite linear diffusion, cyclic voltammetry (CV) through the potential range of concern will yield a peak current $i_{p(rev)}$ given by[15]

$$i_{p(rev)} = 0.4463 \left(\frac{F}{RT}\right)^{1/2} n^{3/2} A\, D_R^{1/2} C_R^* v^{1/2} \quad \textbf{(3)}$$

where F is Faraday's constant (96485.3 coul/mol),

R is the gas constant (8.314 J/mol K),

T is the absolute temperature (298 K),

n is the stoichiometric coefficient of electrons in the redox reaction (1 in this reaction),

A is the planar-equivalent surface area of the electrode (cm^2),

D_R is the diffusion coefficient of VO_2^+, the species being reduced (3.9*10-10 cm2/s)[16],

C_R* is the concentration of VO^{2+} in the bulk solution away from the electrode (0.3 M), and v is the CV scan rate (in V/s).

The geometry of the CF samples tested is far more complex than that which is described by semi-infinite linear diffusion. This geometry was nonetheless used in analysis because: (a) it is the mathematically simplest way of describing three-dimensional diffusion; (b) the long-term response to a potential step applied to a solid CF sample as working electrode showed that current decayed to a true steady-state value until the composition of the electrolyte changed significantly, as expected for semi-infinite linear diffusion, rather than the quasi-steady state current which determines the long-term behavior of cylindrical electrodes[15]; (c) the nature of the deviation between behavior predicted by this analysis and the actual behavior observed is expected to be the same for all samples, since all sample compositions tested had the same bulk structure; and (d) the objective of the analysis is comparison between similar compositions rather than specific measurement of the active area of each sample.

The reduction of V(V) to V(IV) was observed to be slower than fully reversible. For these kinetics, called "quasi-reversible", the peak currents observed in CV are adjusted by adding a term to eq. **(3)**[17]:

$$i_{p(q-rev)} = i_{p(rev)} * K(\Lambda, \alpha) \quad \textbf{(4)}$$

The function K(Λ,α)depends on the transfer coefficient, α, and the combined kinetic parameter **Λ**, which is defined by[17]

$$\Lambda = \frac{k^0}{\left(D_O^{1-\alpha} D_R^{\alpha} Fv/RT\right)^{1/2}} \quad \textbf{(5)}$$

where k^0 is the reaction's standard rate constant (cm/s),

D_O is the diffusion coefficient of VO_2^+, the species being reduced ($3.9*10^{-10}$ m^2/s)[16],

D_R is the diffusion coefficient of VO^{2+}, the reduced species ($3.9*10^{-10}$ m^2/s)[16],

F is Faraday's constant (96485.3 coul/mol),

v is the CV scan rate (in V/s),

R is the gas constant (8.314 J/mol K), and

T is the absolute temperature (298 K).

The combined kinetic parameter **Λ** can be calculated if all the values in eq. **(5)** are well known, but an easier and more common means of measurement, called the Method of Nicholson[18], provides a means of acquiring **Λ** from the potential difference between the forward and reverse peaks. This offers a rapid means of estimating k^0 as well.

Once **Λ** and α are known, the value of K can be determined, as related by Matsuda and Ayabe[17]. Those authors offer the following graph as a means of quickly estimating values of K. For the redox reaction of eq. **(1)**, α has been reported to be 0.5.[19]

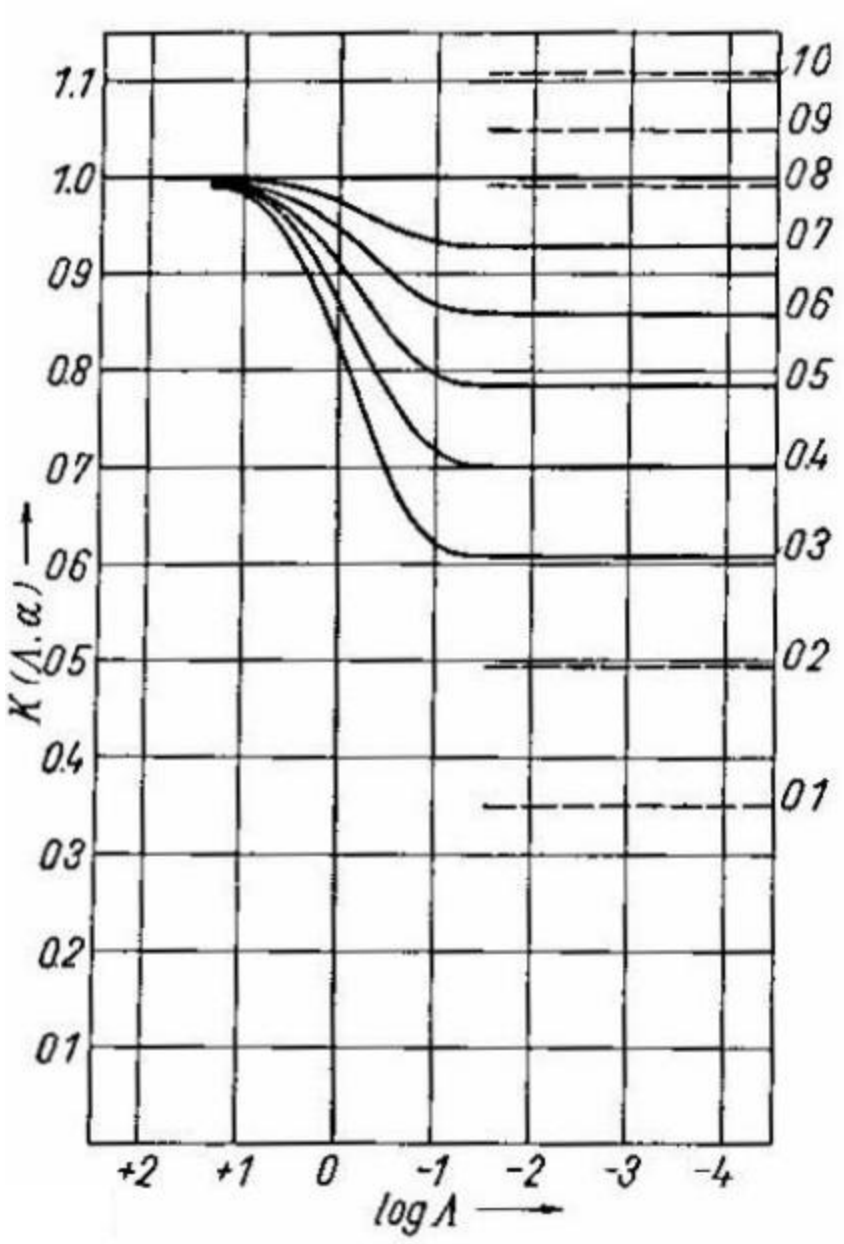

Fig. 1.2 Variation in K with **Λ** for some values of α, shown on the right side of the graph. Fig. 4 in ref. 17.

From Fig. 1.2, it is seen that the parameter K will be between about 0.78 and 1. The value of **Λ** changes with scan rate, per eq. **(5)**, but slowly. If all other parameters in eq. **(5)** are held constant, the scan rate must change by a factor of 10,000 for the value of K to change between 1 and its stable value for low **Λ** values. Because the scan rates used in this experiment are

relatively close together, spanning a single decade, the value of K will be treated as approximately constant for a CV experiment with a single sample. This predicts that a graph of peak current vs. square root of scan rate will be linear, with a slope that can be related to the area, though because it does not account for the value of K (approximated as constant), this will be an "electroactive area" and not a true area value. The true area value can be estimated from electrochemical data by approximating the value of K for an experiment, averaged over all cycles.

For each sample tested, a cyclic voltammetry program was run under various scan rates (0.5, 0.6, 0.7, 0.8, 0.9, 1, 2, 3, 4, and 5 mV/sec) in the voltage range 1.6 V to 0.5 V vs. SCE. The peak current of each cycle was recorded as $i_{p(q\text{-}rev)}$. The average value of K can be used to adjust the slope to its equivalent reversible value, which can be related to the area by rearranging eq. **(3)**:

$$\frac{i_{p(rev)}}{v^{1/2}} = A\left[0.4463\left(\frac{F^3}{RT}\right)^{1/2} n^{3/2} D_R^{1/2} D_R^*\right] \textbf{(6)}$$

The bracketed term is equal to 0.1587 amps $(V/s)^{-1/2}$ cm^{-2}. This measured area is related to the sample mass for each type of impregnated felt, and the area per mass is used to compare the electrocatalytic effectiveness of each sample, which is reported as electroactive area per mass.

Further analysis can reveal more detailed information about the heterogeneous rate constant of the vanadium redox reaction, following the methods of Nicholson[18]. The forward and reverse peak potentials are compared, and their difference is recorded as ΔEp. When the standard heterogeneous rate constant is sufficiently high, or when the scan rate v is sufficiently slow, the system follows reversible kinetics, and ΔEp = 60/n mV[18]. By increasing the scan rate, the system exhibits quasi-reversible kinetics, where value of ΔEp increases with $v^{1/2}$. Specifically, the value of ΔEp can be related to the combined kinetics parameter Ψ, defined as

$$\boldsymbol{\Psi} = \frac{\boldsymbol{k^0}}{\left(\pi D_O^{1-\alpha} D_R^{\alpha} Fv/RT\right)^{1/2}} \textbf{(7)}$$

(which differs from the definition of $\boldsymbol{\Lambda}$ defined above by only a factor of $\boldsymbol{\pi}^{-1/2}$). Eq. **(7)** can be rearranged as

$$\boldsymbol{\Psi} = \left[\left(\frac{\boldsymbol{D_O}}{\boldsymbol{D_R}}\right)^{\boldsymbol{\alpha/2}} \left(\frac{\boldsymbol{RT}}{\boldsymbol{\pi D_O F}}\right)^{\boldsymbol{1/2}} \boldsymbol{k^0}\right] \textbf{(8)}$$

so that, in the quasi-reversible region, the slope of Ψ vs. $v^{-1/2}$ can be used to find the value of the rate constant k^0 for the system.

All sample compositions were measured by EIS to probe the nature of charge transfer at the various interfaces. Based on the SEM images, it is hypothesized that charge transfer must occur in two potentially limiting steps: at the interface between the electrolyte and the surface of the oxide layer, and between the oxide layer and the carbon felt. The simplified equivalent circuit model which was used represents four processes in series:

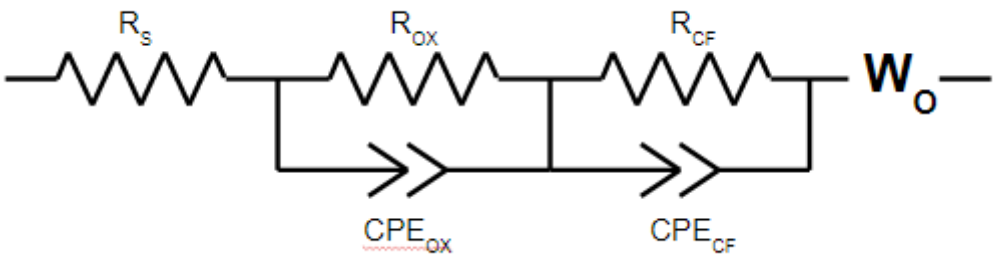

Fig. 1.3 Simplified circuit model for EIS

The resistance R_S (Ω) represents the uncompensated solution resistance, which is a consequence of the distance between the tip of the reference electrode and the center of the bulk mass of the working electrode.[15] This was minimized by locating the working and reference electrodes as close together as possible. Variations in the measured value of R_S are due primarily to sample bulk geometry and experimental variation, and were not taken to be analytically significant.

The first charge transfer process, between reducing ions in the electrolyte and the surface of the Nb_2O_5 nanocrystals of the working electrode, is represented by the two parallel elements R_{OX} and CPE_{OX}. R_{OX} represents the charge transfer resistance of this process, modeled as an ideal, linear resistance. CPE_{OX} represents the effective capacitance of the electrochemical double layer in solution that results from this charge transfer resistance. For the purposes of EIS measurements, the capacitance of this process is not well modeled by an ideal, linear capacitor, and the component used instead is a "Constant Phase Element", so called because the phase angle of this capacitance is independent of signal frequency.[20]

A CPE is described by two parameters. CPE-T (F) is roughly equivalent to a capacitance value. CPE-P is a unitless exponent which describes the extent to which the CPE impedance deviates from the impedance of an ideal capacitor. The extent of non-ideality manifests on a Nyquist plot as raising or lowering the impedance arc of an ideal capacitor. When CPE-T = 1, the CPE behaves as an ideal capacitor.

The second charge transfer process occurs between the Nb_2O_5 layer and the carbon felt, and is represented by a charge transfer resistance R_{CF} and a non-ideal capacitance CPE_{CF}. In all samples, this process dominated the overall charge-transfer kinetics, likely due to the low conductivity of Nb_2O_5. Some compositions tested showed significant changes in one charge transfer resistance relative to the other; see discussion below.

The final circuit element is called a Generalized Finite Warburg element, which was used to model the diffusion process of ions through an electrically non-conducting electrolyte. The Warburg-Open type circuit element is described by three parameters. WO-R (Ω) is a scaling factor analogous to diffusion resistance. WO-T (s) is equivalent to a diffusion time, which can be

expressed as WO-T = L^2/D_O, where L is the diffusion length and D_O is the usual diffusion coefficient. WO-P is a unitless power parameter similar to the CPE non-ideality factor. These parameters were modeled, but generally showed high uncertainty values, and were omitted from the analysis of the EIS data. In reality, there are more processes that occur in the electrochemical cell, such as charge transfer at the counter electrode and conduction between the carbon felt and platinum wire of the working electrode, which could be modeled in theory; however, the shapes of these processes did not manifest in the EIS plots that were developed experimentally, indicating that charge transfer at these interfaces was too facile to be measured.

As shown in the SEM images above, the oxide coverage of the felt was incomplete, and some patches of bare carbon felt were exposed to the electrolyte, and participated in the vanadium reduction reaction. It has been shown elsewhere that properly treated carbon felt can be an effective catalyst to this reaction.[7] This process operates in parallel with the niobium pentoxide-carbon felt series of charge transfers. A more complicated circuit model including this process is shown in Fig. 1.4, in which R_{Bare} represents the charge transfer resistance between vanadium ions in solution reducing at the surface of the exposed carbon felt, and CPE_{Bare} represents the portion of the capacitance of the solution double layer located around the exposed carbon felt patches. Fitting the measured data to a circuit of this complexity was infeasible, since no practical means of determining the exposed bare carbon felt area or the fraction of oxide coverage could be found. Thus, this circuit was not used.

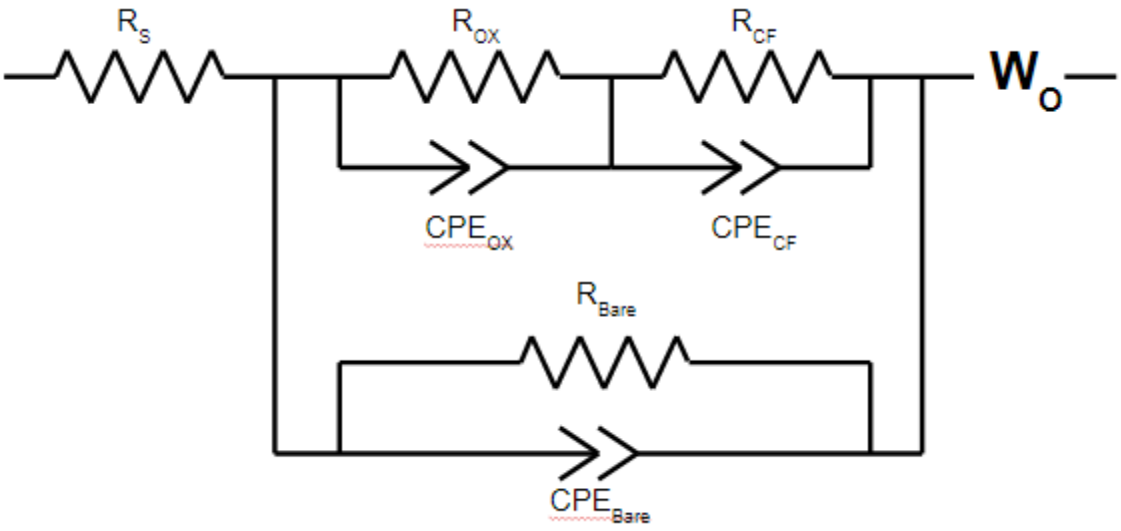

Fig. 1.4 Alternate circuit model for EIS

Chapter 2. EXPERIMENTAL

2.1 SYNTHESIS

Carbon Felt

The precursor solutions are prepared by combining the desired masses of Ammonium Niobium Oxalate (ANO), Ammonium Paratungstate (APT), Ammonium Titanyl Oxatale (ATO), Ammonium Molybdate (VI) Tetrahydrate (AMT), and Ammonium Zirconium Carbonate (AZC) in DI water and mixing via magnetic stirring for two hours. The tungsten precursor APT was slowest to dissolve in all samples.

The ANO and APT were purchased in the form of solid powders, and the AZC in the form of an aqueous solution, from Sigma Aldrich. The ATO and AMT were purchased in the form of solid powders from Acros Organics.

Carbon felt samples (Rongke Power) are rinsed in DI water and thermally activated in an oxygen atmosphere at 420°C for 3 hours. Small carbon felt rectangles are placed in teflon autoclave vessels, which are then filled with the mixed precursor solution and sealed. These vessels are heated in a muffle oven at 170°C for 48 hours, with a ramp rate of 5°C/min. Once the vessels are cooled, the carbon felt samples are removed and rinsed thoroughly in DI water and then ultrasonicated in DI water for 1 hour, and are subsequently dried in a drying oven. The samples are then heated in a tube furnace at 10°C/min to a calcination temperature of 500°C for two hours under argon flow, and are then oven cooled in static argon until below 100°C, at which point they are stored in ambient atmosphere, in plastic bags.

Electrolyte

The V(V) electrolyte was prepared by dissolving the required mass of V_2O_5 in a solution of 5M H_2SO_4 in DI water under magnetic stirring, at room temperature, in a sealed glass container. The approximate dissolution time was four days.

The solid V_2O_5 was purchased as a solid powder from Aldrich Chemical Company, Inc. The $VOSO_4$ was purchased as a solid powder from Alfa Aesar. The concentrated H_2SO_4 solution was purchased from EMD Millipore Corporation.

2.2 CHARACTERIZATION

Small pieces of prepared impregnated carbon felt were tested electrochemically in a three-electrode cell, using a platinum wire as the counter electrode, a saturated calomel electrode (SCE: CHI150, CH Instruments) as the reference electrode, and carbon felt held in place by platinum wire as the working electrode. Electrochemical testing for electroactive area was performed on an ARBIN BT-G test station. EIS measurements were performed using a Solartron SI 1287 Electrochemical Interface with an SI 1260 Impedance/Gain-Phase Analyzer.

All compositions in this work were tested for stability in the electrolyte by placing carbon felt samples in a simulated electrolyte (5 M H_2SO_4 in water solution) for two days. The felt samples were weighed, dry, before and after this treatment and all samples had consistent mass. The electrolyte was boiled down and the residue collected and weighed, and this mass was never significant.

Surface area was measured using a Quantachrome NOVA 4200e surface area and pore size analyzer. All samples tested in this way were prepared by vacuum degas at 300 °C for at

least 16 hours, as recommended by the equipment manufacturer; however, samples showed no difference in mass due to the degassing process, which would have been expected.

XRD was performed using a Bruker D8 Focus . Powder samples were prepared for XRD measurements as follows. The desired mass of carbon felt (approximately 200 mg) was cut from a larger sample, and ground by mortar and pestle with a small amount (approximately 2-3 mL) of isopropyl alcohol. This created a uniform slurry, which was dried in air at 85 °C in a vented oven. This slurry was collected and mildly agitated by metal spatula to be packed on a glass plate for diffraction analysis.

SEM images were taken on a JEOL JSM-6010 Plus/LA. Except where noted, SEM samples were prepared by grinding small amounts of carbon felt to dust with a razor blade, and applying that dust to carbon tape and affixed to an aluminum stud.

Measurements of the mass of deposited material required physically separating the implanted metal oxide mass from the carbon felt. Separation was achieved by heating samples to 900 °C for 60 minutes in static air, which removed all carbon from the sample. The remaining mass was collected and weighed. This procedure maintained the overall bulk metal oxide structure, though presumably not its crystal structure. Post-combustion samples retained the overall shape of the carbon felt substrate.

Chapter 3. RESULTS AND DISCUSSION

3.1 SEM

The carbon felt used in synthesis has significant surface features. Some of these features are present in the as-delivered felt, and the thermal activation process exacerbates surface roughness by removing mass through slow combustion.

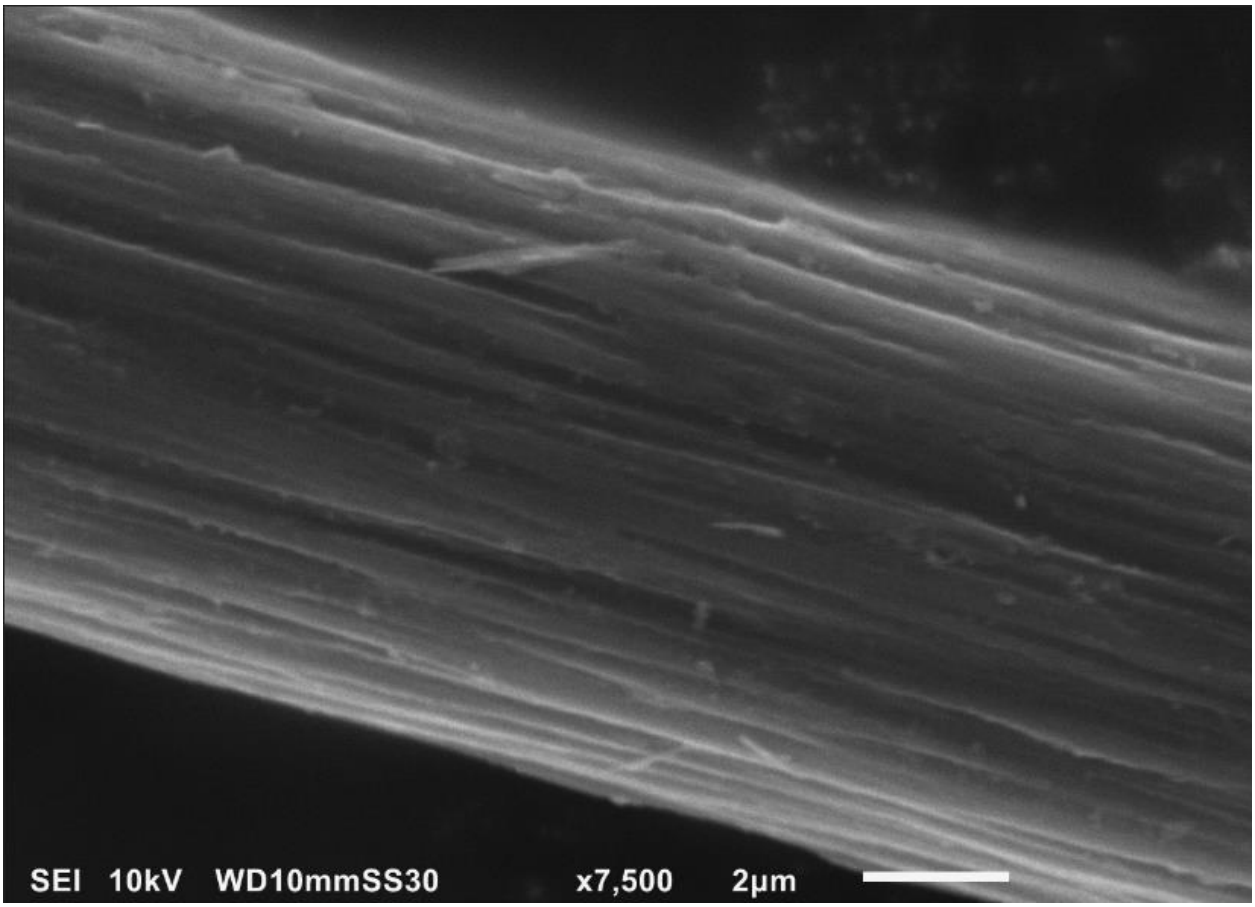

Fig. 3.1 Thermally activated carbon felt with no intentionally deposited mass

SEM images of the felt before and after the thermal activation process did not show significant differences in the felt surface, though experimentally it was noted that the activated

carbon felt is very hydrophilic, wetting instantly, whereas the as-delivered carbon felt is mildly hydrophobic, which makes hydrothermal synthesis ineffective. Experiments which impregnated non-activated carbon felt with oxide mass showed such poor electrochemical performance that they were discarded without further characterization.

Previously published work on niobium pentoxide as an electrocatalyst on carbon felt for use in vanadium redox flow batteries, Li et al.[12], produced highly crystalline, high surface area clusters of nanorods, distributed across the carbon felt surface.

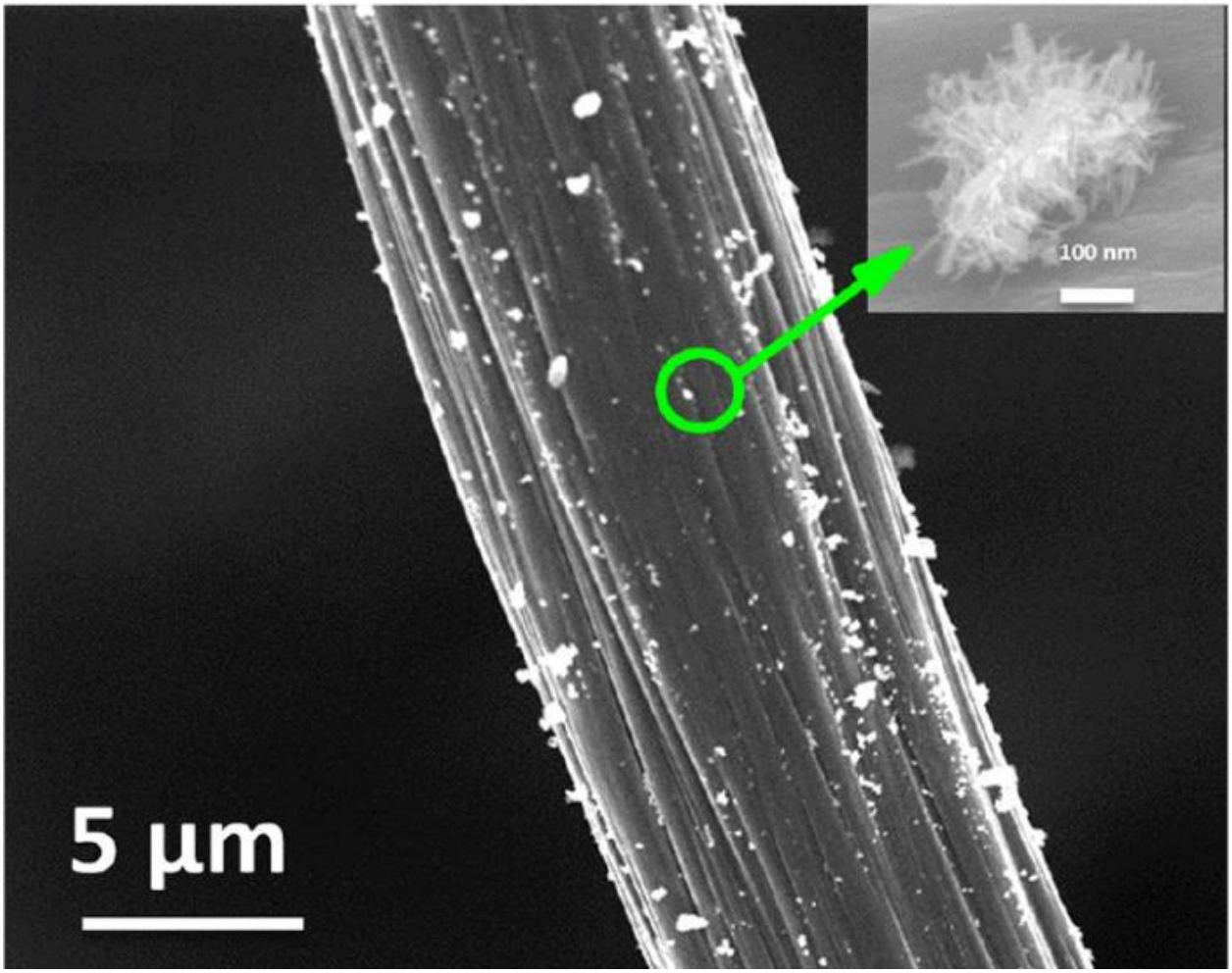

Fig. 3.2 Nb_2O_5 nanocrystals on carbon felt, Fig. 2(d)[12].

Following the work of Li et al. in the general procedure of sample preparation, the morphology found by those authors was expected, but could not be achieved. Instead, samples of all compositions, including the composition of some samples discussed by Li et al., showed continuous coverage of the carbon felt surface by the oxide layer, punctuated by oxide dendrites or other structures. This morphological difference likely accounts for the difference in electrochemical effectiveness of those samples, as discussed below.

In all samples produced and tested for this work, the oxide layer was continuous, though the oxide layer coverage on the carbon felt surface was incomplete. SEM images showed that, for all tested compositions, sporadic patches of carbon felt were not covered by the oxide layer. No means of measuring the fraction of the carbon surface covered by the oxide layer could be found. Because the SEM sample preparation method required grinding the felt samples into individual fibers, and because the oxide mass is highly brittle, the SEM images may underrepresent the oxide layer coverage.

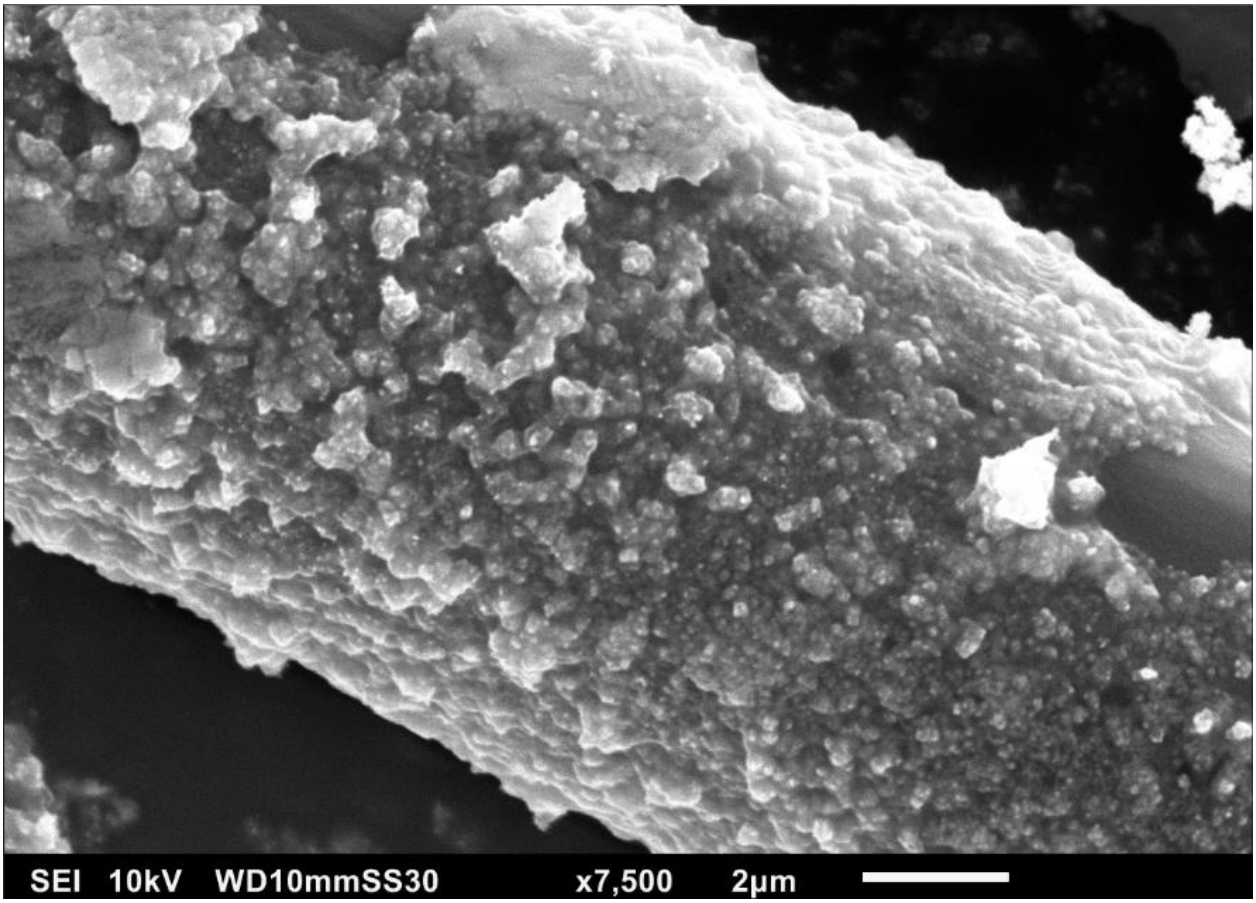

Fig. 3.3 Oxide layer coverage and morphology of (10 w/o W)-Nb_2O_5 on activated carbon felt. This sample was sputter coated with 40% gold, 60% palladium to resolve the surface more clearly. (All other images are from samples that were not sputter coated.)

The morphological disparity between the samples prepared in this work and the samples of previous work indicates some substantial difference in preparation. The synthesis procedure reported by Li et al. used a small volume of aqueous precursor solution to submerge carbon felt in a teflon sealed autoclave which was then heated for 48 hours. The authors refer to "white solid precipitates" in the teflon vessel and on the carbon felt surface which were collected by vacuum filtration for analysis, which is taken to mean that the vessel was dry at the end of the hydrothermal synthesis process. It is unclear how a sealed vessel filled with aqueous precursor

solution would become dry during this process unless the teflon vessels were unsealed or leaked steam when heated. All samples in this work, prepared by the methods laid out in Sec. II, had significant fluid remaining in the autoclave vessels, and although some showed a noticeably lower fluid level, this was rare and the volume of fluid lost was never greater than about 5 mL of the 25 mL teflon vessel volume.

The addition of more than 1 w/o of either of the tetravalent dopants tested, titanium or zirconium, differed from the bulk structure of (W, Mo) or (W)-doped Nb_2O_5. These samples showed a thin, smooth oxide layer on most of the carbon felt surface, with much larger crystals which were more sporadically distributed.

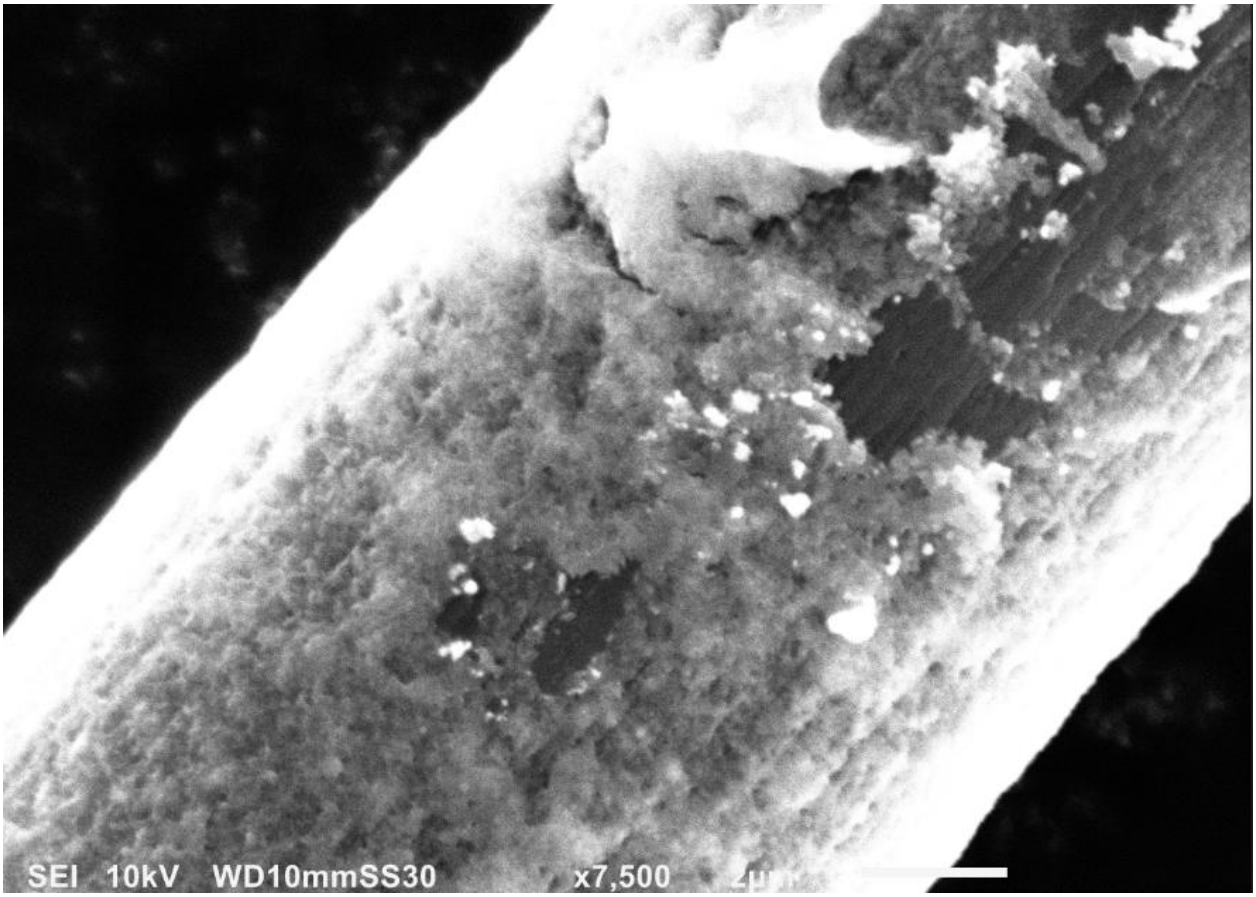

Fig. 3.4 Discontinuity of oxide coverage on carbon fiber for (10 w/o Ti, 10 w/o W)- Nb_2O_5

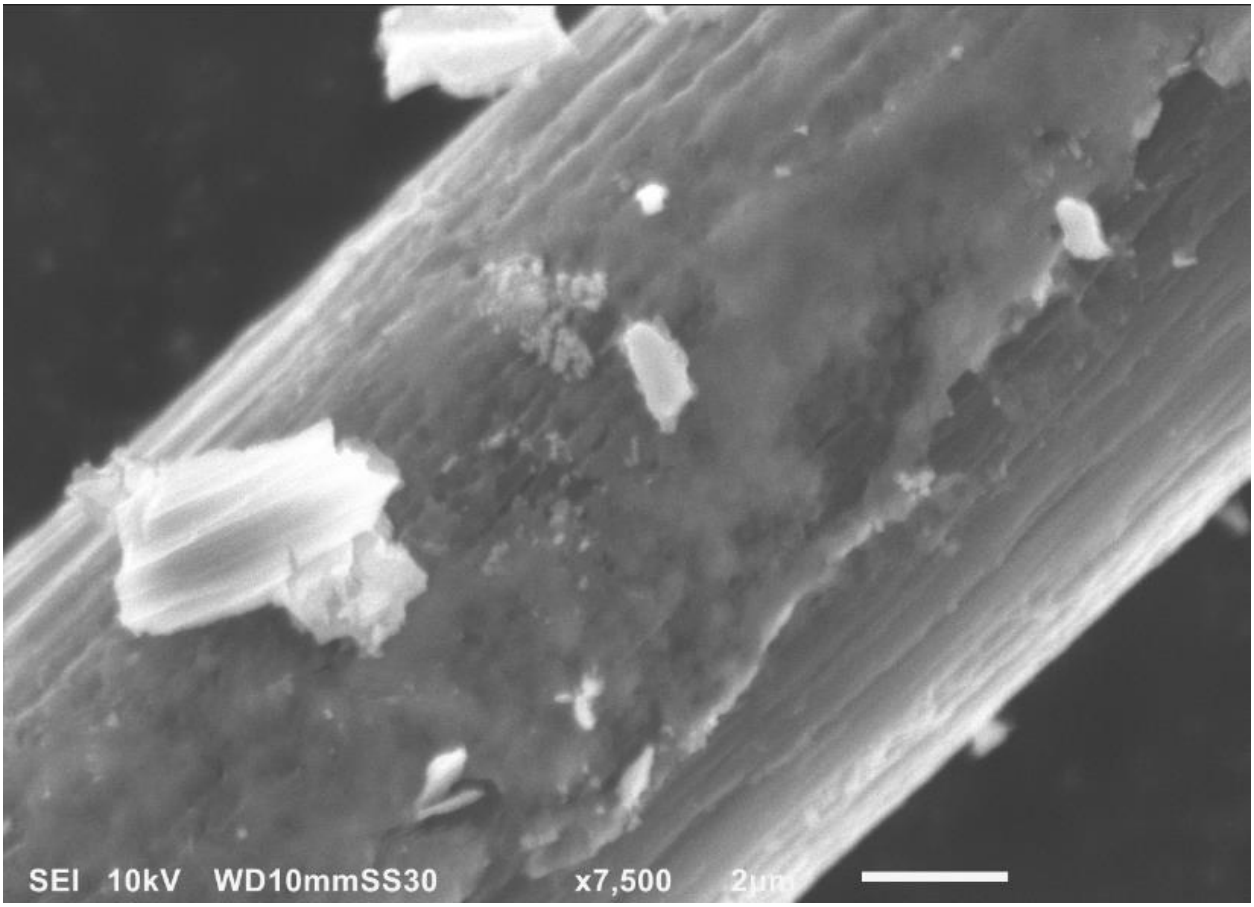

Fig. 3.5 Surface morphology of (10 w/o W, 10 w/o Zr) Nb_2O_5

These images may be underrepresenting the amount of large crystals attached to the carbon felt surface in these samples. Sample preparation for SEM images involved disintegrating the sample and distributing the powder on carbon tape, which separated much of the large crystal mass from the carbon fibers. Images of these samples at lower magnification show large masses which were mechanically separated in this way.

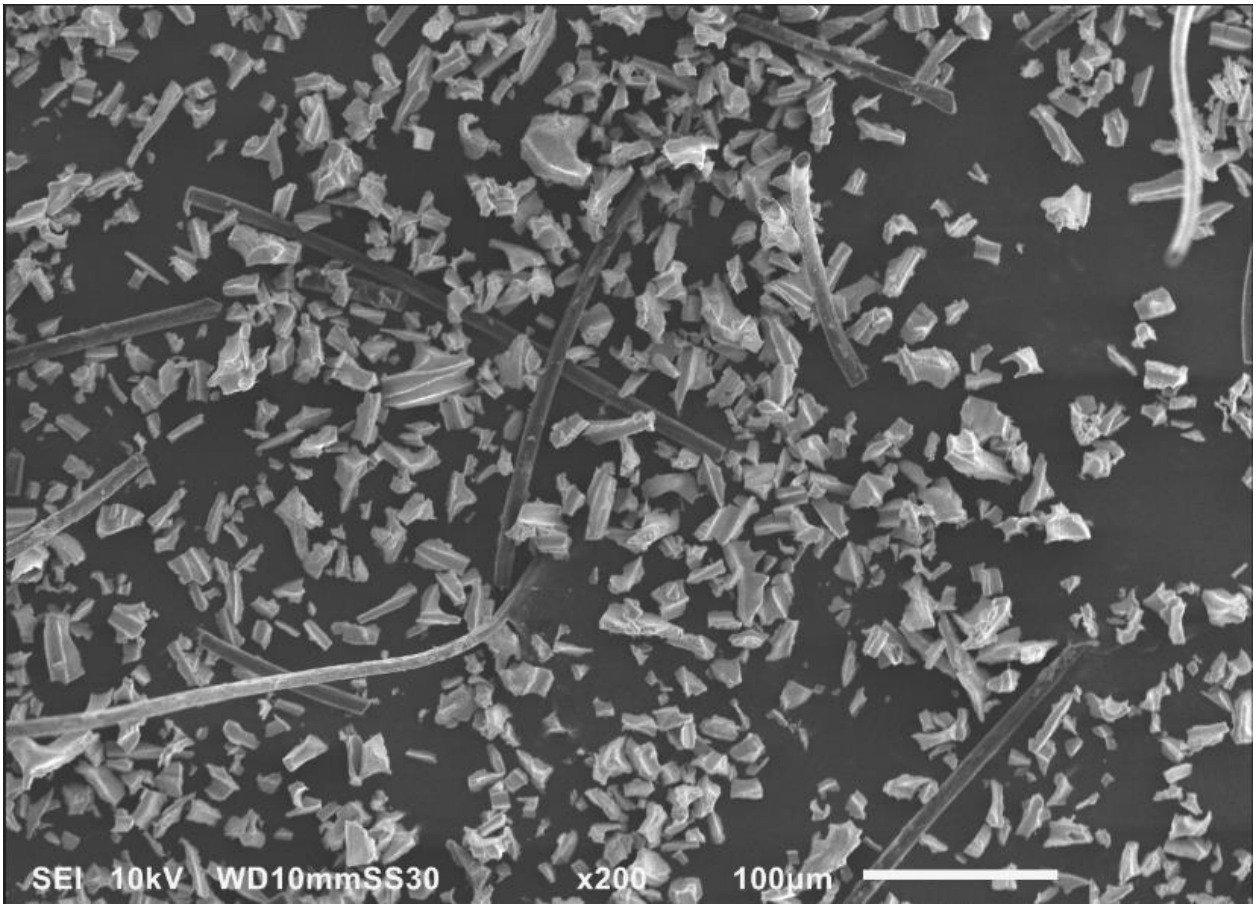

Fig. 3.6 Carbon fibers and separated crystalline mass for a sample of (10 w/o Zr, 10 w/o W)-Nb_2O_5. The black background is carbon tape used in sample preparation.

To investigate the amount of mass removed by sample preparation for SEM imagery, one sample was viewed with almost no mechanical manipulation after synthesis. The bulk felt was imaged, shown here. (Note that the random orientation of carbon fibers makes it difficult to resolve very much area, and most of the image is out of focus as a result. For the same reason, only limited magnification yielded clear images.) The amount of removed mass does not appear to be significant.

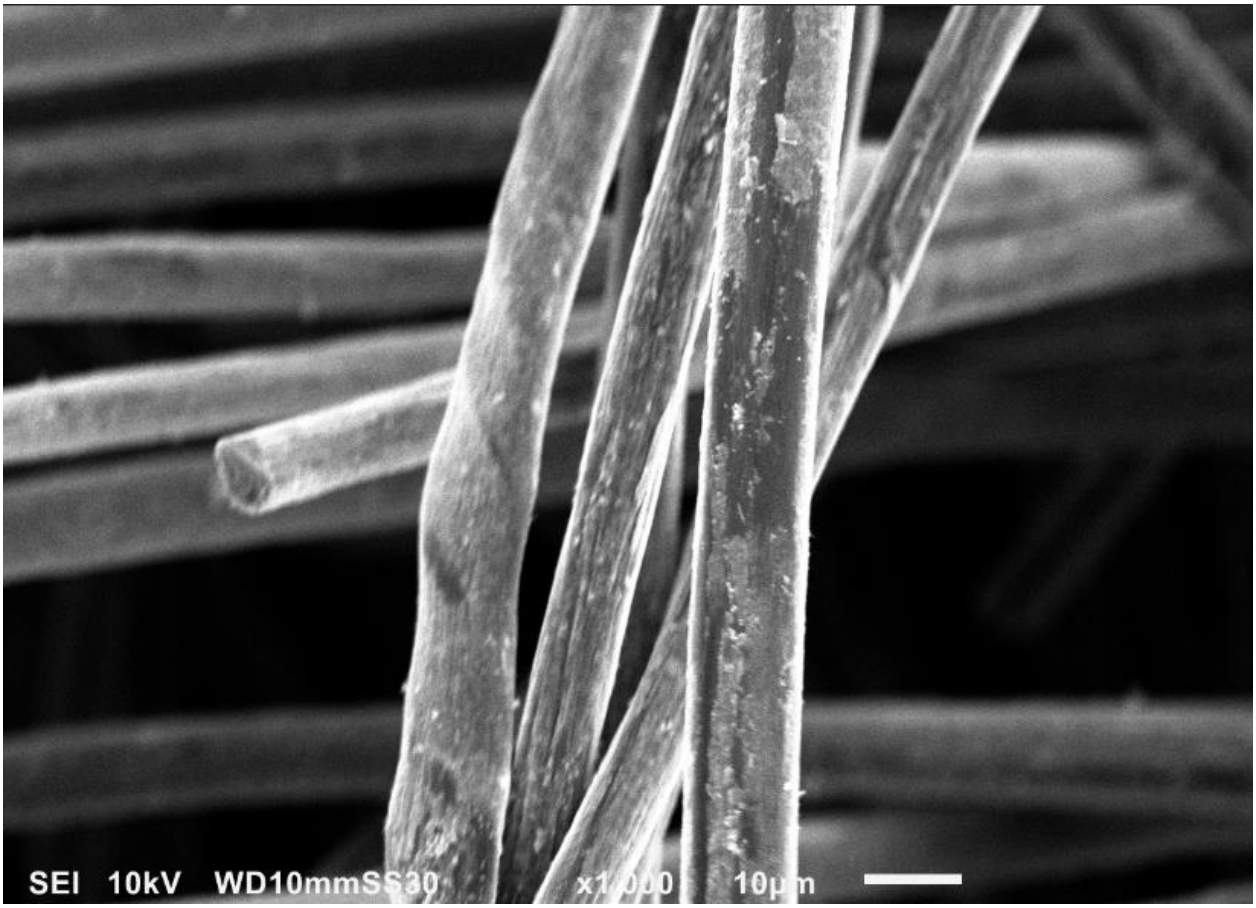

Fig. 3.7 Morphology of deposited material on carbon fibers with minimal agitation in preparation. Sample composition was (10 w/o W, 5 w/o Zr)-Nb_2O_5

Samples of any dopant tested at the 1 w/o level had morphology that appeared very similar to the (10 w/o W) Nb_2O_5. This is reasonable, as that level of impurity could be expected to be incorporated into the Nb_2O_5 structure without radically changing the structure. One example is depicted here.

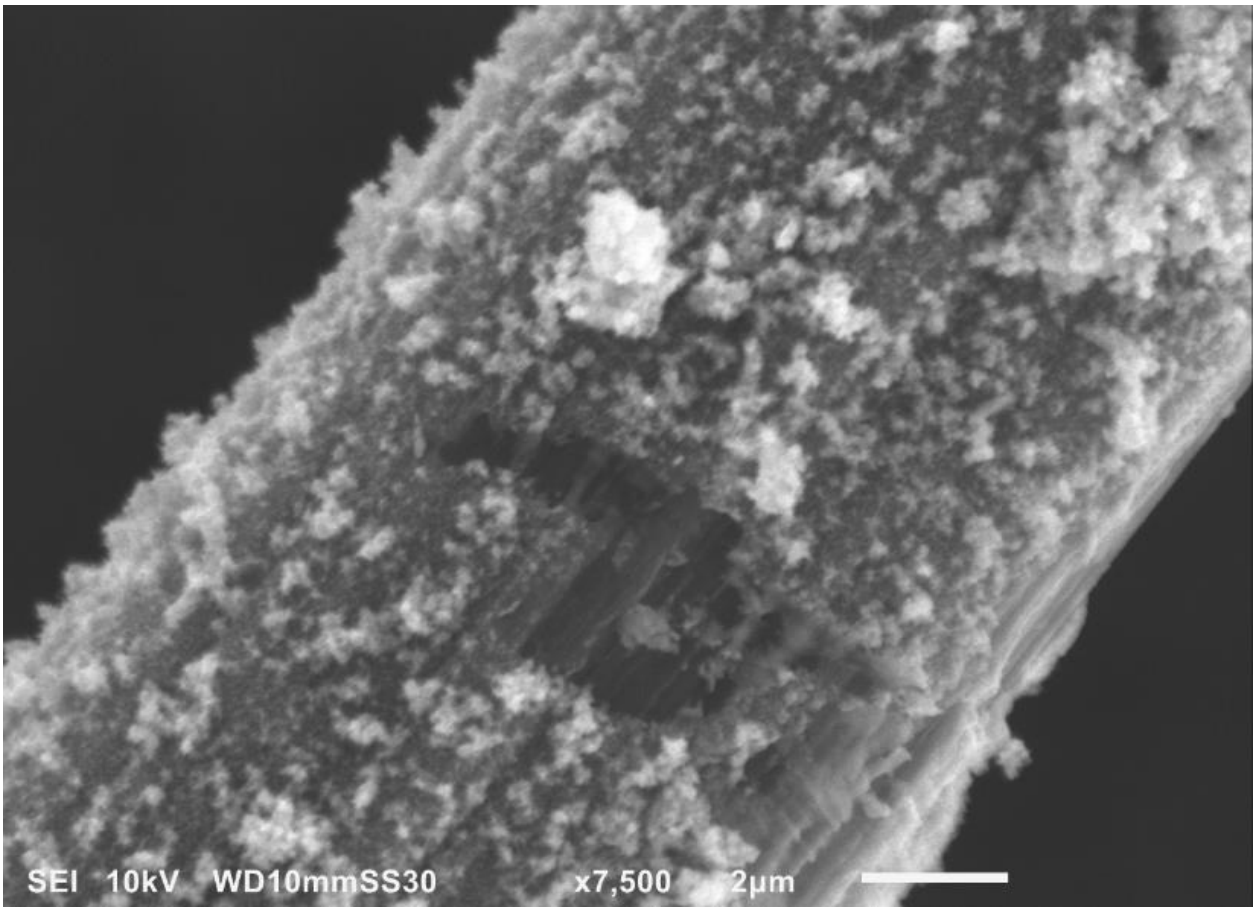

Fig. 3.8 Surface morphology of (10 w/o W, 1 w/o Mo) Nb_2O_5

The overall morphology of samples doped with 5 or 10 w/o Mo was seen to be inconsistent from SEM images. Some areas had a smooth layer coating most of the carbon felt with sporadic patches of crystalline protuberances, and some areas were indistinguishable from (10 w/o W)-Nb_2O_5. Both of these morphologies appeared in the same sample.

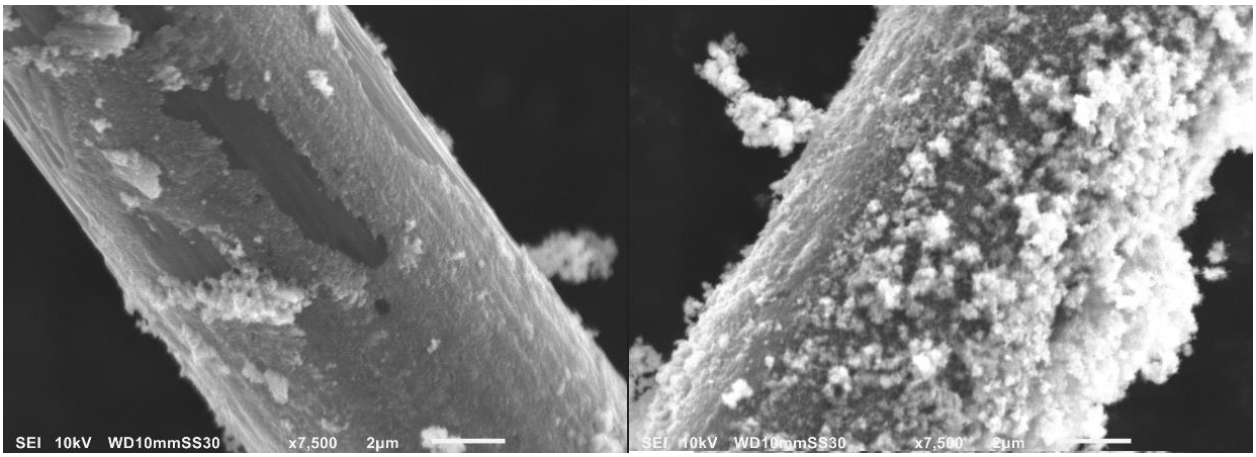

Fig. 3.9 Surface structure variation in a single sample of (10 w/o W, 5 w/o Mo)-Nb_2O_5

The total mass deposited on the carbon felt varied with sample composition. Undoped and Mo-doped Nb_2O_5 showed generally higher levels of deposited mass than Ti-doped or Zr-doped Nb_2O_5.

Table 3.1 Mass deposited on carbon felt samples for all tested compositions.

	Ti	Mo	Zr
10 w/o	3.1	10.2	9.0
5 w/o	3.1	9.5	4.3
1 w/o	9.8	10.7	11.1
(10 w/o W)-Nb_2O_5	11.9		

From the above, molybdenum doping seems to have very little effect on the hydrothermal deposition process, consistent with the SEM images. The effect of titanium seems to be to reduce the amount of deposited material up to some limit between 1 and 5 w/o and to have no further effect.

The odd trend in mass deposition for zirconium is persistent across many samples tested.

Note that deposited mass was determined with minimal mechanical manipulation of samples; in samples with larger and fewer deposited bodies, such as 10 w/o Zr, it is possible that large crystalline masses not bonded to the carbon felt surface may have been mechanically bound to the carbon felt bulk, which may cause overestimation of the mass of deposited material. It is possible that zirconium encourages the growth of non-crystalline bodies during the hydrothermal synthesis, and that many of these particles are removed from a sample with 5 w/o Zr during the rinsing and ultrasonication steps, but that the growth rate is faster at 10 w/o Zr to the extent that these masses become large enough to be mechanically stuck in the carbon felt bulk, and not removable by rinsing.

3.2 XRD

Because the oxide mass was measured in the presence of the graphite substrate, a background measurement was made of activated carbon felt, prepared for analysis in the same manner as all other XRD samples. The surface of the powder sample was not ideally smooth, resulting in an elevated background intensity at low 2θ values.

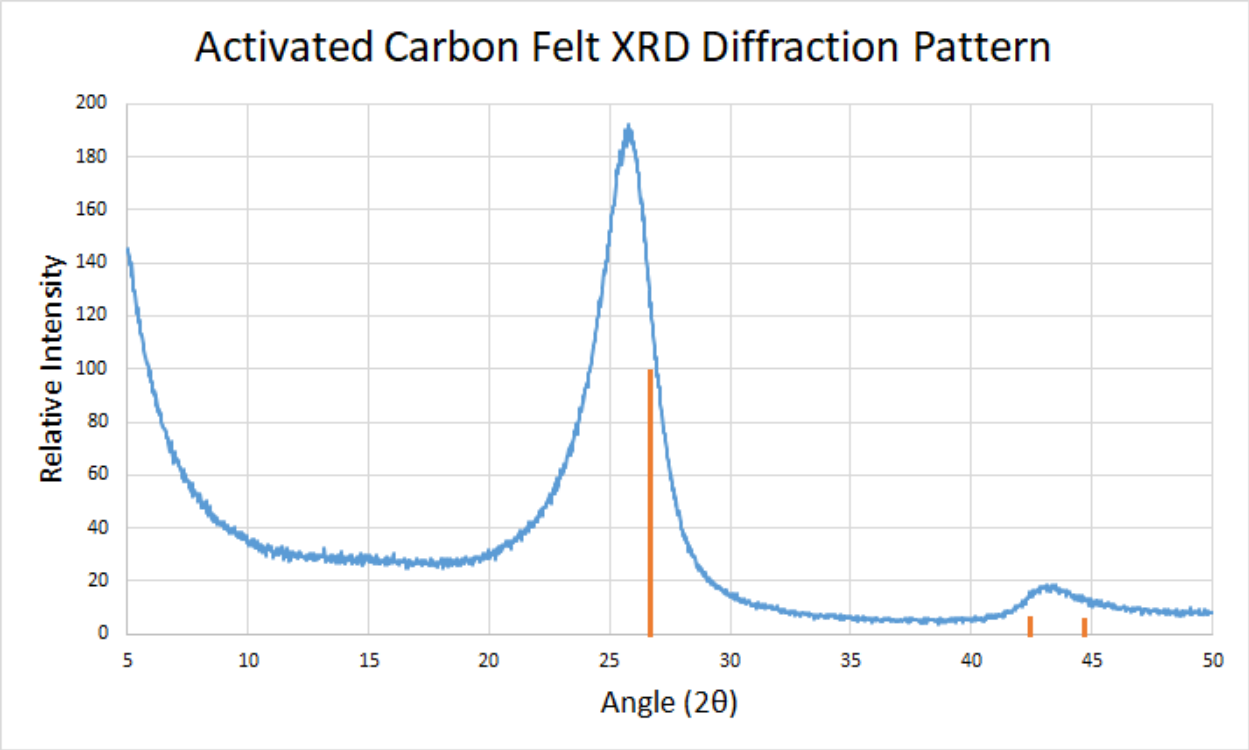

Fig. 3.10 Diffraction pattern for powdered activated carbon felt, with no added oxide material, with known peak locations for graphite[21] superimposed. The major peak is shifted from the literature value by 0.76° (2θ).

Further XRD patterns have their low-angle background intensities removed for clarity. The (10 w/o W) Nb_2O_5-impregnated carbon felt showed an additional peak just below the major peak for graphite, at 2θ=23°.

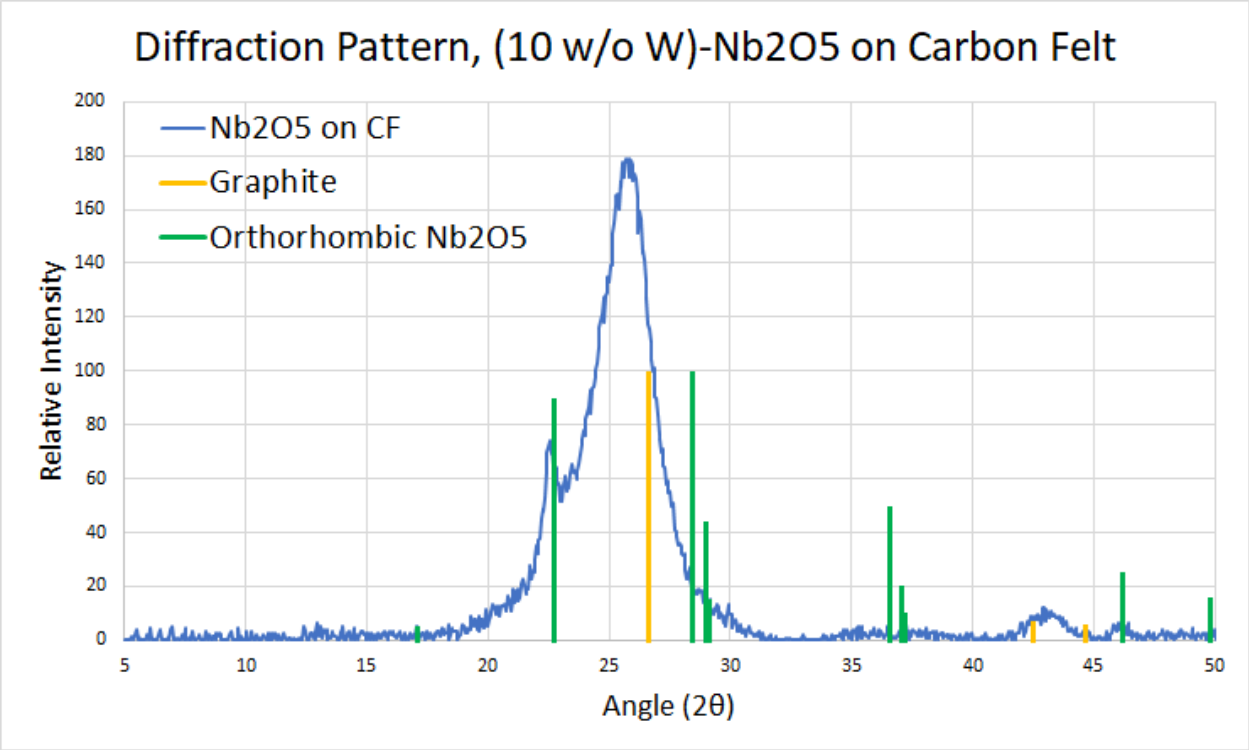

Fig. 3.11 XRD for (10 w/o W) Nb_2O_5-impregnated carbon, background intensity removed, with the XRD pattern for the orthorhombic phase of Nb_2O_5 [22]

For the compositions with Ti, Mo, and Zr doping, no peaks were noted other than those seen in Figs. 3.10 and 3.11. The presence and level of these dopants seemed to change only the amount of orthorhombic Nb_2O_5 present, consistent with the deposited mass measured in Table 3.1, and no new crystal structures were observed.

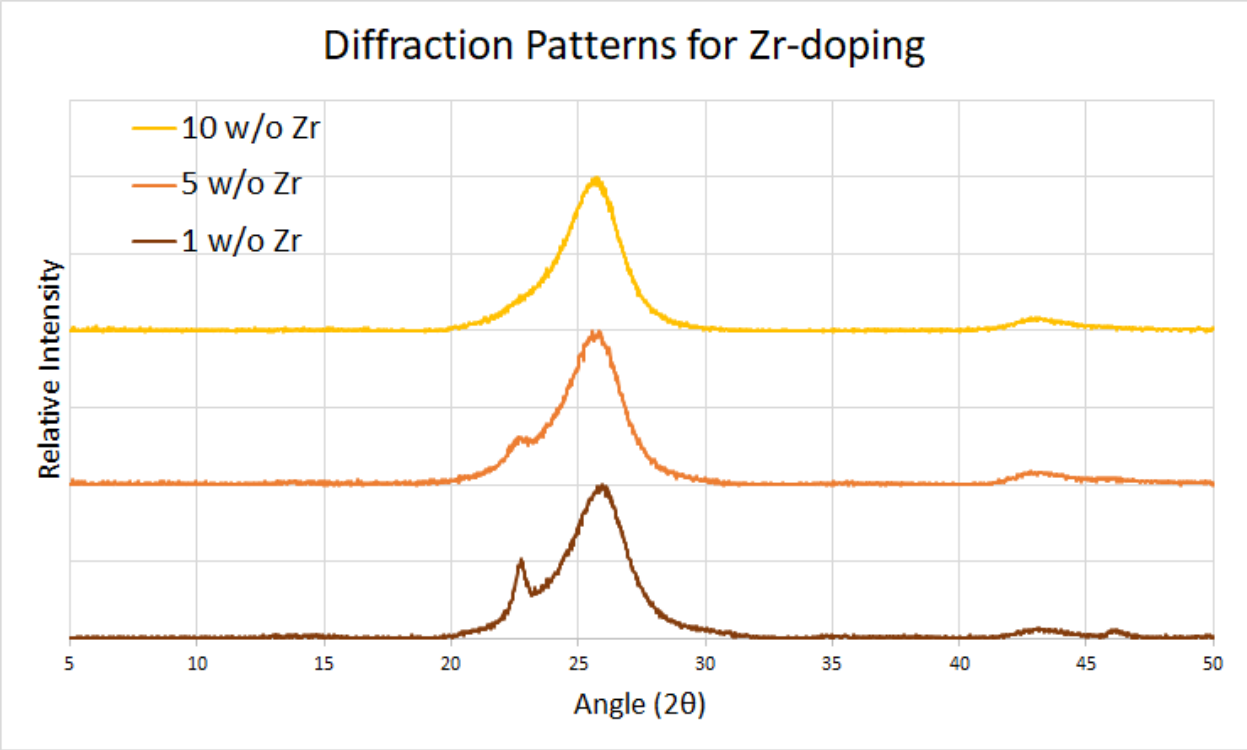

Fig. 3.12 XRD results for 10, 5, and 1 w/o Zr-doped Nb_2O_5 on carbon felt

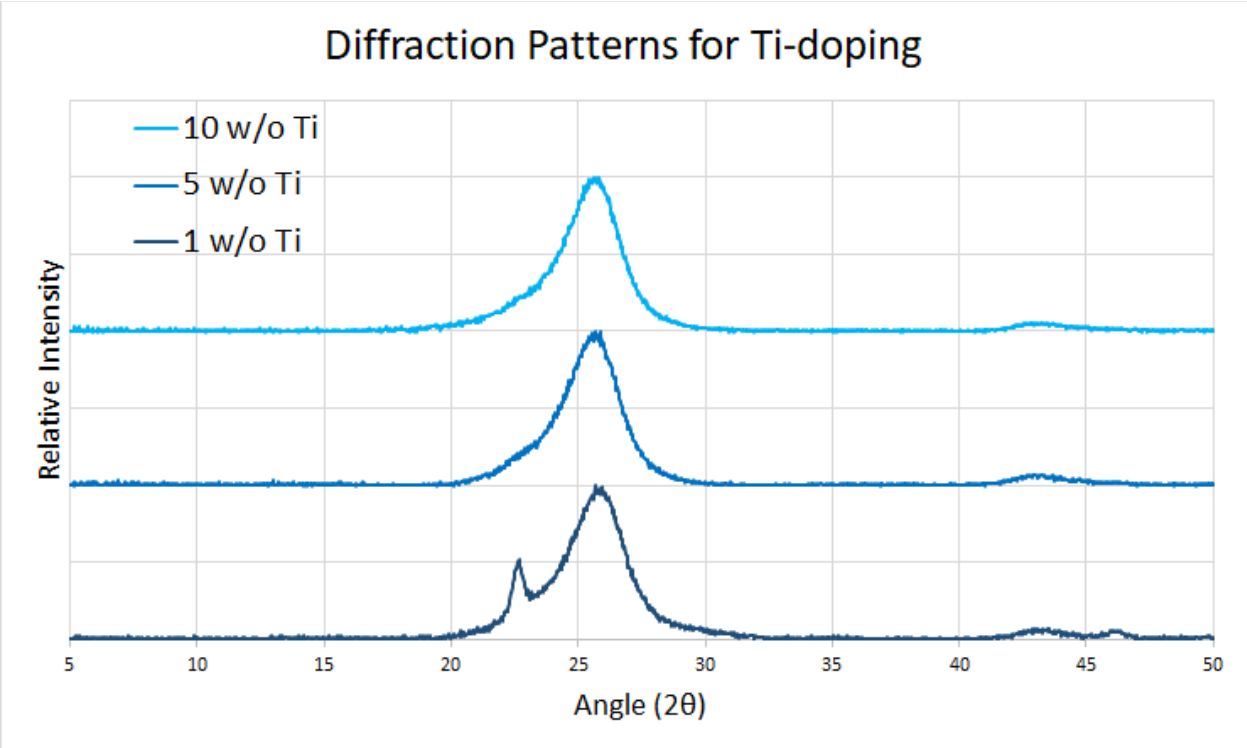

Fig. 3.13 XRD results for 10, 5, and 1 w/o Ti-doped Nb_2O_5 on carbon felt

For samples doped with titanium and zirconium, increasing the dopant level seems to decrease the amount of orthorhombic Nb_2O_5, which is consistent with the measurements of deposited mass. For both Zr and Ti at the 10 w/o concentration, the diffraction patterns are nearly indistinguishable from bare carbon felt. The deposited mass, then, must be mostly amorphous.

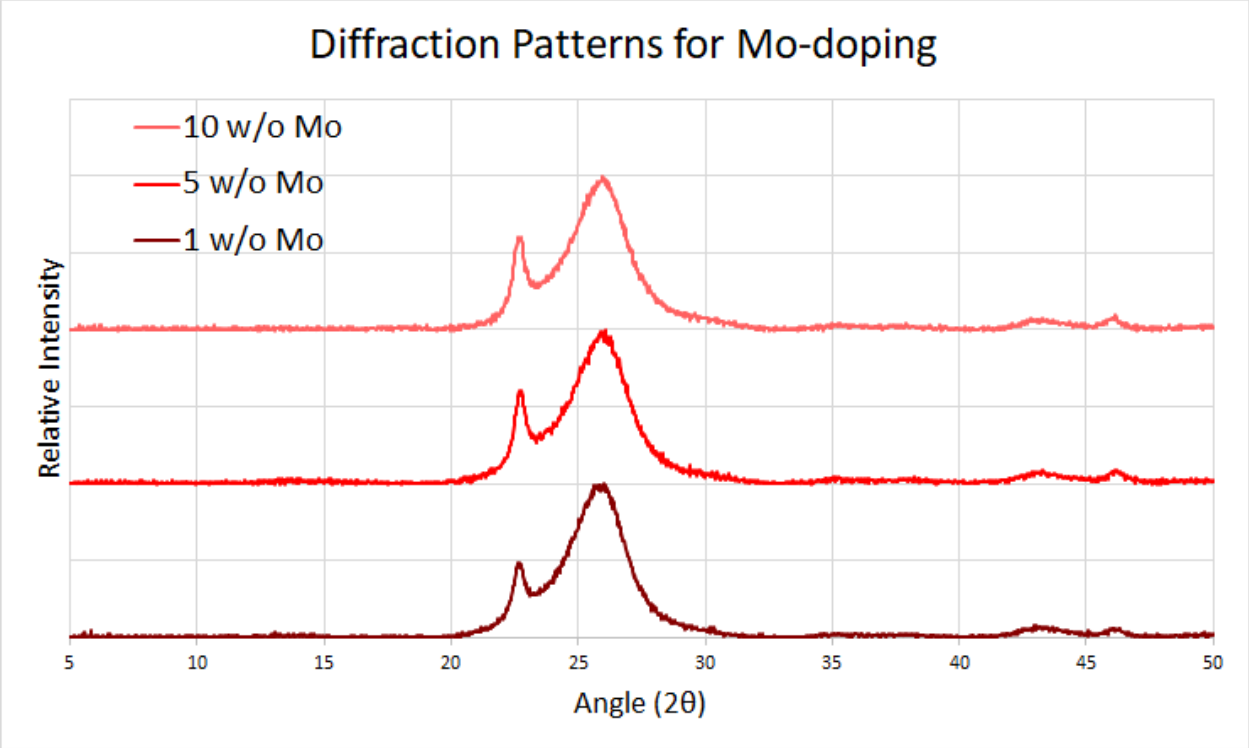

Fig. 3.14 XRD results for 10, 5, and 1 w/o Mo-doped Nb_2O_5 on carbon felt

For the molybdenum doped samples, all dopant levels showed about the same peak intensity for the identifying peaks for orthorhombic Nb_2O_5 at about the same intensities. Consistent with the deposited mass, the presence of molybdenum seems to have no large-scale effect on the morphology or hydrothermal deposition of Nb_2O_5 on carbon felt.

3.3 CYCLIC VOLTAMMETRY

Each CV test used the same set of scan rates (0.5, 0.6, 0.7, 0.8, 0.9, 1, 2, 3, 4, and 5 mV/sec) in the same voltage range, 1.6-0.5 V. The normal single-peak CV curve results were observed for most samples. The results of a representative test are shown here.

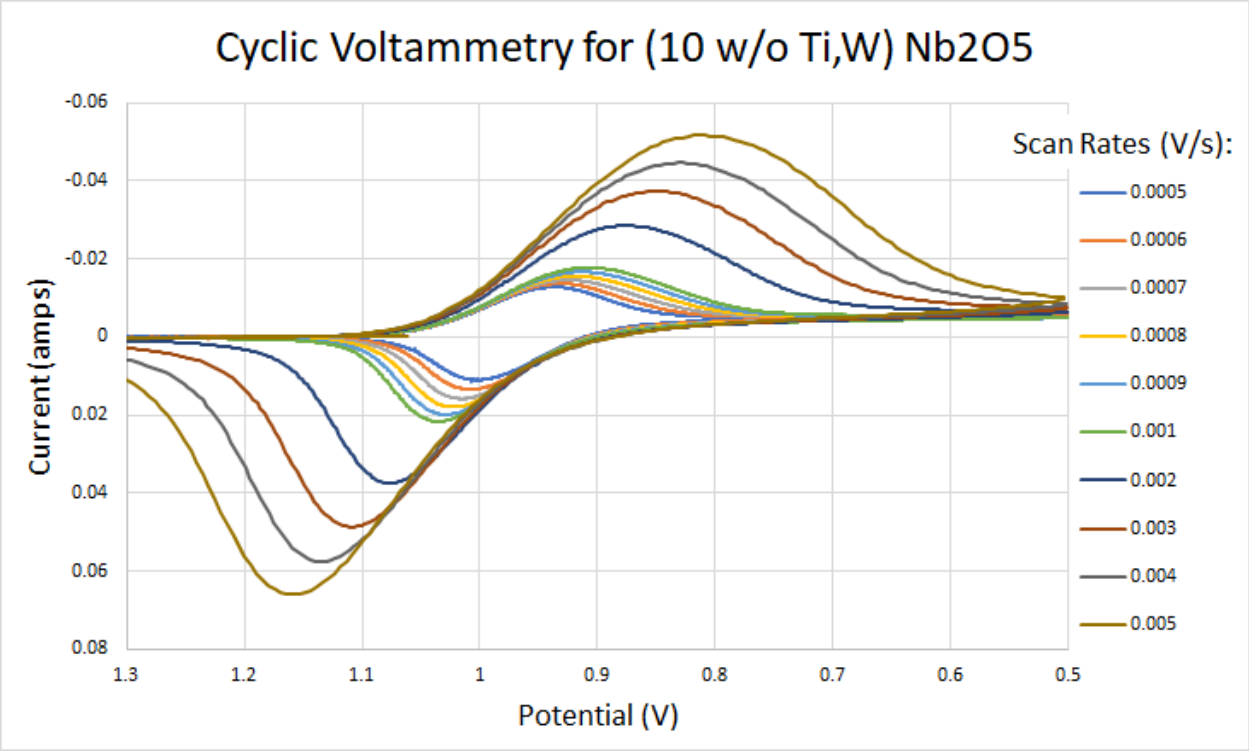

Fig. 3.15 Cyclic Voltammetry for a sample of 0.0076 grams of carbon felt impregnated with Nb_2O_5, with 10 w/o tungsten and 5 w/o titanium

A background test was run for each cell used for analysis, using the standard electrolyte and no carbon felt. In all cells, and all potentials and scan rates, the background current was never higher than 50 μAmps, and was usually less than 5 μAmps, which is close to the detection limit of the machine in the current detection range used. In these experiments, current did not peak as it would in an experiment like that in Fig. 3.15, indicating that vanadium redox did not

occur at a significant rate on the surface of the platinum electrodes. For this reason, a background current correction was not made for the CV tests.

Using the result of eq. **(8)**, measured values of i_{peak} for each cycle were plotted vs. the square root of the scan rate $v^{1/2}$ for several samples of each sample composition. A sample plot of this type is shown here.

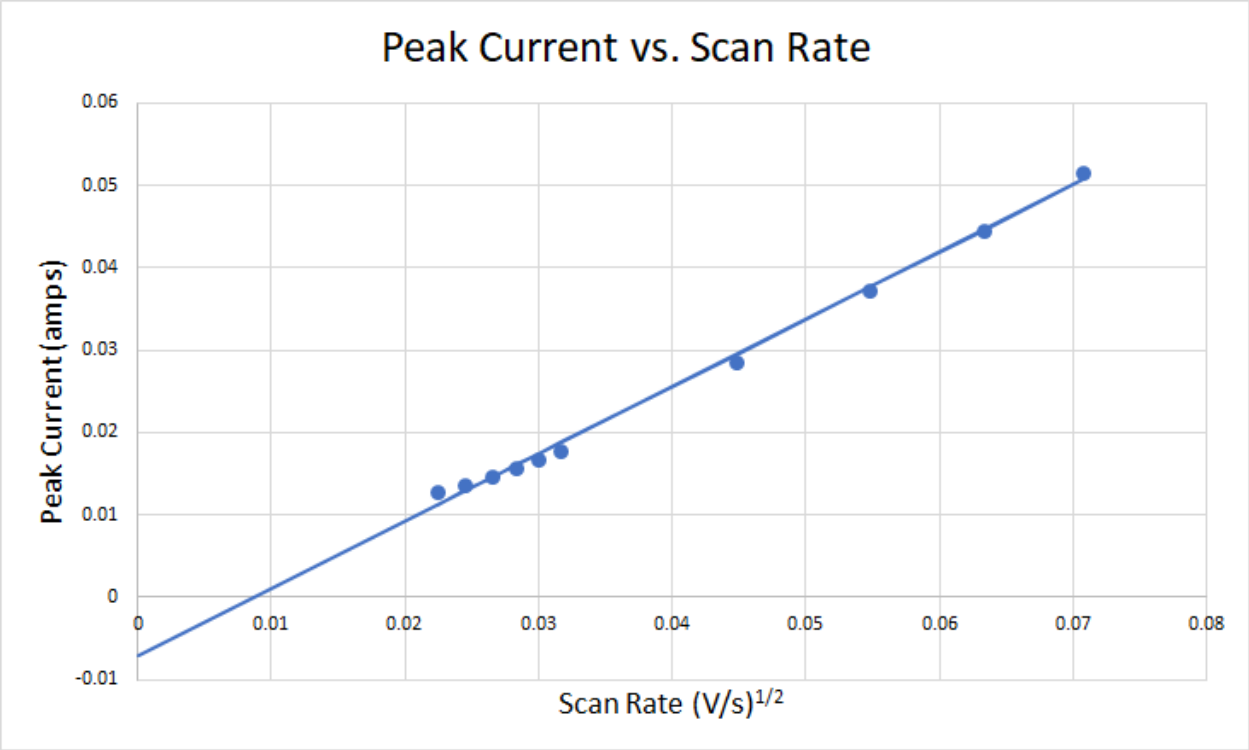

Fig. 3.16 Peak current vs. square root of scan rate for all cycles shown in Fig. 3.15

These plots generally showed a strongly linear trend; however, some samples with a high effective area showed reversible or nearly reversible kinetics at the slowest scan rates. In this kinetic region, peak currents were higher than would be predicted by a strictly linear relationship, and the data deviated positively from the linear trend. In this region, the parameter K changes with scan rate, which manifests as a slight curvature in the lower scan rates. The reversibility of

kinetics was observed through the difference in potentials between the forward and reverse peaks. In CV for reactions which exhibit fully reversible kinetics, the expected peak splitting potential difference (difference between forward peak potential and reverse peak potential) is 59/*n* mV at 25 °C.[15] In faster cycles, the value of peak splitting increased in an approximately linear fashion (plotted against the square root of scan rate), as shown here. The grey line is placed at the reversible value of 59 mV. (For V(V) reduction, *n*=1.)

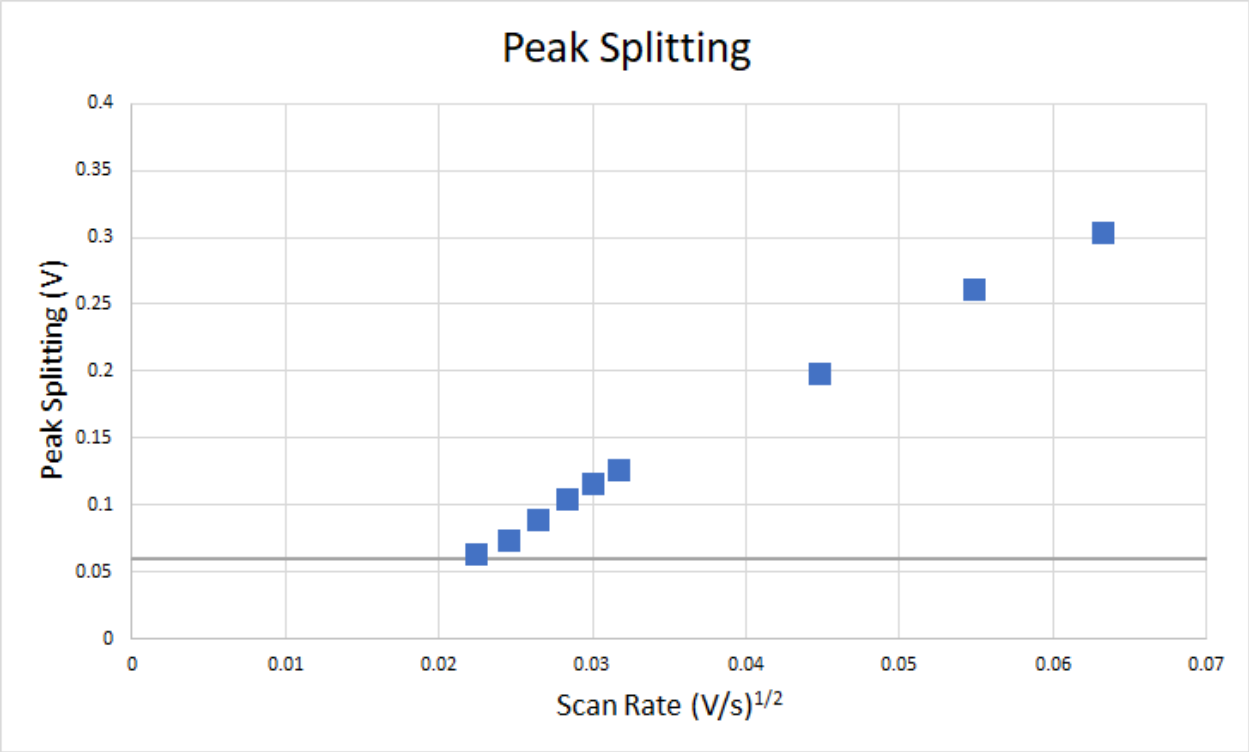

Fig. 3.17 Peak splitting vs. square root of scan rate for the same sample as Figs. 3.15-16

Due to this deflection at slow scan rates, the y-intercept was generally not zero. The slope used to measure electroactive area was not calculated by enforcing a zero-intercept for this reason. In samples which showed slow kinetics and low electroactive area, all cycles were far from reversible and the linear fit of the data was stronger and had an intercept very close to zero.

One example of this is shown here. In these samples, the cycle behavior was never near-reversible, and the value of K was constant over multiple scan rates.

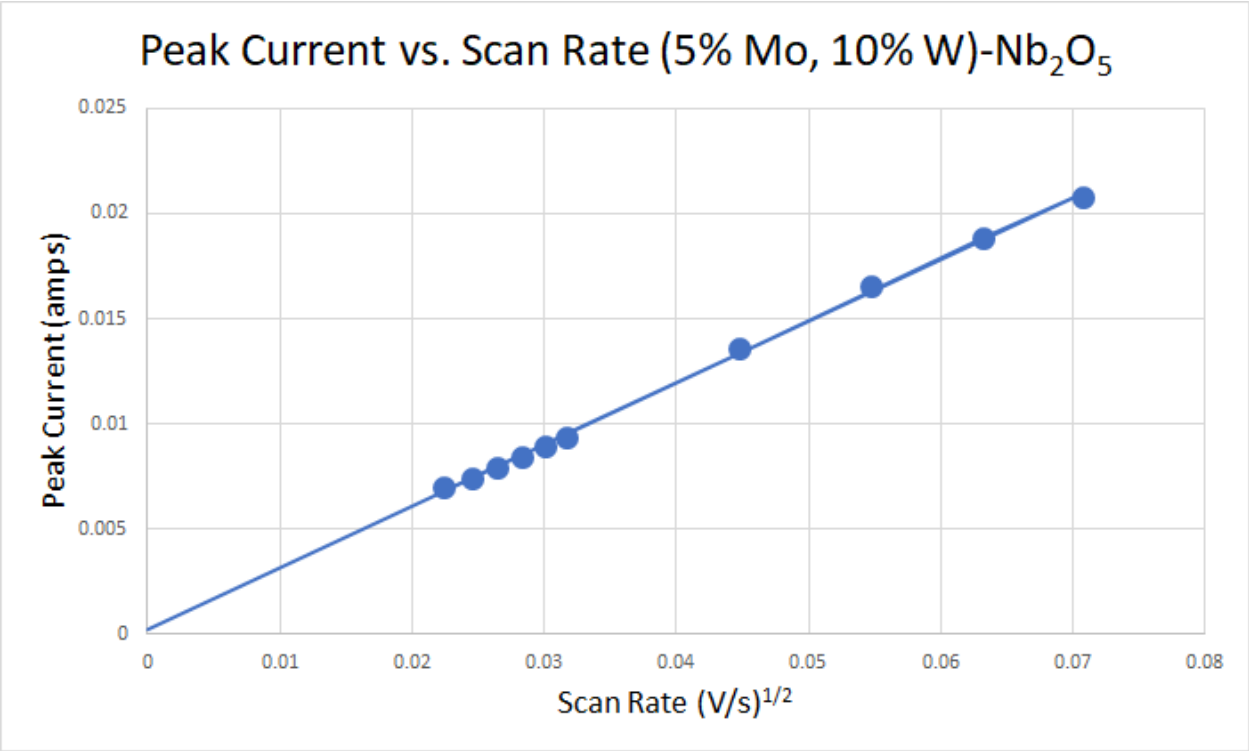

Fig. 3.18 Peak current plotted against square root of scan rate for a sample that did not show a significant deviation due to nearly-reversible kinetics at slow scan rates. Sample mass was 0.0102 grams. Y-intercept for this trendline is $2.5*10^{-4}$ amps.

This analysis was repeated for at least five felt pieces cut from each of at least three different prepared samples of felt. This effective area per sample mass, averaged over the tested samples, is summarized in the table below. Samples were also made and tested without tungsten; see discussion below.

Table 3.2 Summary of Electroactive Area for Samples of All Concentrations

(values reported as 10^2 cm^2/gram)

	Ti	Mo	Zr
10 w/o	5.15	3.46	5.11
5 w/o	5.47	1.81	5.19
1 w/o	2.85	1.63	1.54
10 w/o (no W)	4.63	1.29	5.15
10 w/o W only	1.74		
Bare carbon felt	5.98		

As a control, the electroactive area of several samples of (10 w/o W) Nb_2O_5-CF using this method was found to be $1.74*10^2$ cm^2/gram. The electroactive area is plotted here against sample mass for five pieces of one sample, with a superimposed linear fit line. For each composition, the above data comes from the sample which was used for the graphs below. These specific samples were selected as being representative of their respective compositions, and similar electroactive areas were measured among other samples of the same composition.

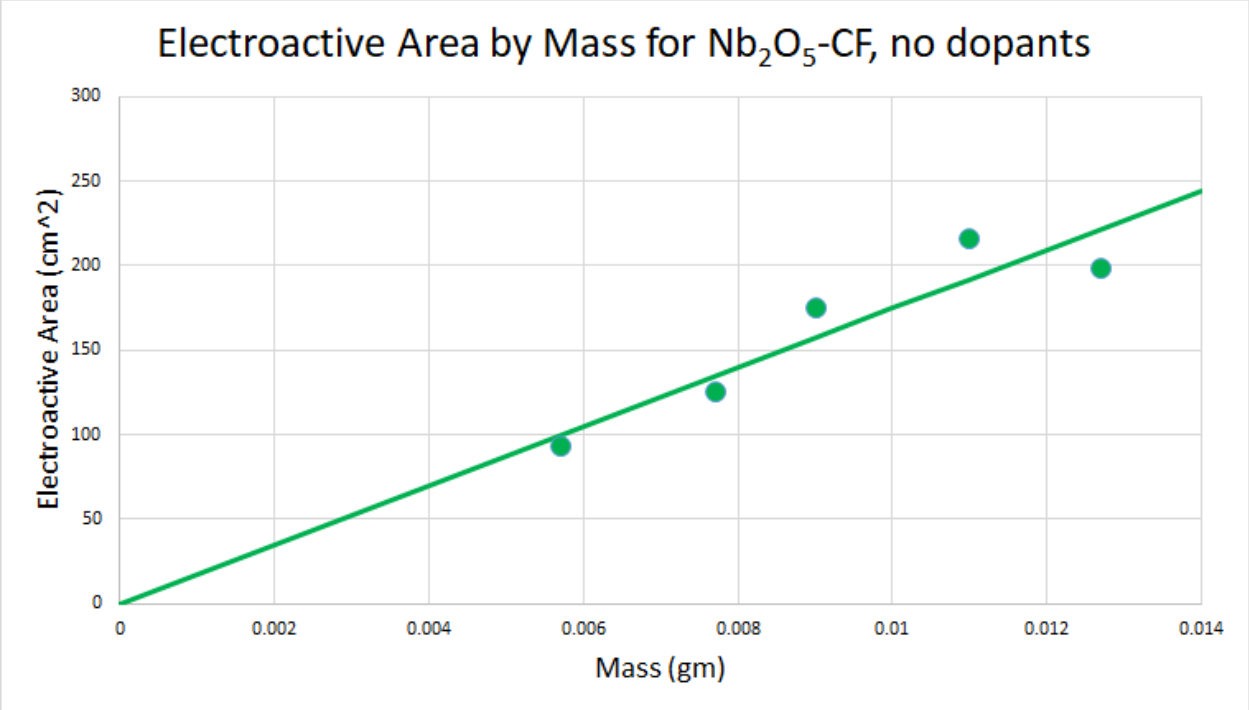

Fig. 3.19 Linear fit describing relationship between electroactive area and sample mass for (10 w/o W)-Nb_2O_5 impregnated carbon felt

The mass range which could be effectively characterized by the sample apparatus was about 0.0050 grams to 0.0150 grams. Below the lower limit, samples of carbon felt tended to disintegrate when handled or affixed to the working electrode. Above the upper limit, all sample compositions tested deviated negatively from the strong linear trend in area per mass, toward a stable measured area independent of mass. This could be because larger samples had more carbon felt mass that was not near the platinum wire of the working electrode, and not necessarily in electrical contact with the potentiostat circuit.

Li et al.[12] demonstrated significant improvement in the catalytic effectiveness of Nb_2O_5-impregnated carbon felt vs. activated carbon felt, toward the vanadium redox reaction of eq. **(1)**. Those results could not be reproduced, as previously discussed, which could be due to the

morphological difference between their samples of dispersed crystal clusters and the morphology found in this work. The electroactive comparison between activated carbon felt and the same felt with (10 w/o W) Nb_2O_5 mass deposited was unfavorable.

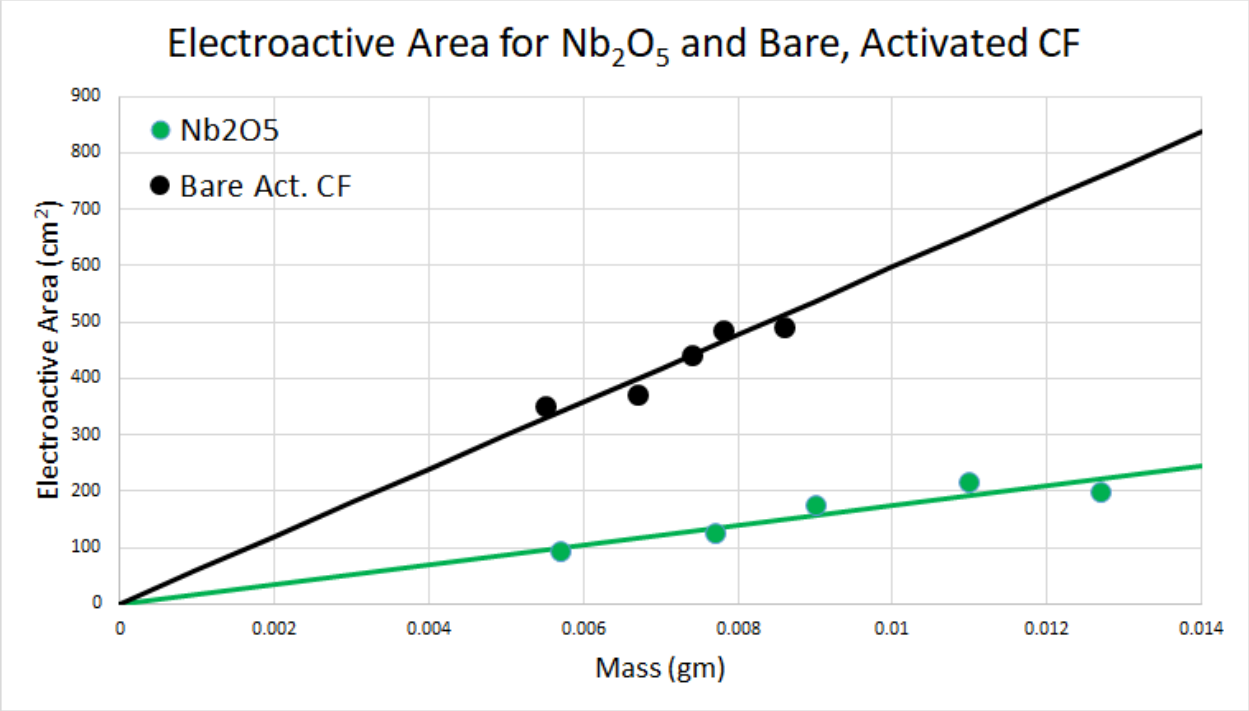

Fig. 3.20 Linear relationship between electroactive area and mass for samples of (10 w/o W)-Nb_2O_5 impregnated carbon felt and bare activated carbon felt

The activated CF electroactive area was found to be $5.98*10^2$ cm^2/gram, which was higher than even the most effective samples with deposited oxide mass, though not by a high degree. Because the goal of this work was improvement in electrocatalytic effect by the use of dopants to improve conductivity and charge-transfer resistances, all results were compared to the Nb_2O_5-impregnated carbon felt, to judge the effectiveness of dopant addition at these specific concentrations.

The samples which were doped with titanium showed an increase in effective area per mass relative to the (10 w/o W) Nb_2O_5-impregnated carbon felt samples. The 1 w/o dopant level showed only a slight improvement in electroactive area, and the 5 and 10 w/o dopant levels showed significant improvement. The difference between the 5 and 10 w/o Ti samples was slight, consistent across multiple samples made from the same precursor solution compositions, which may indicate that the solubility limit for titanium in the Nb_2O_5 nanostructures is reached at some level between 1 w/o and 5 w/o Ti.

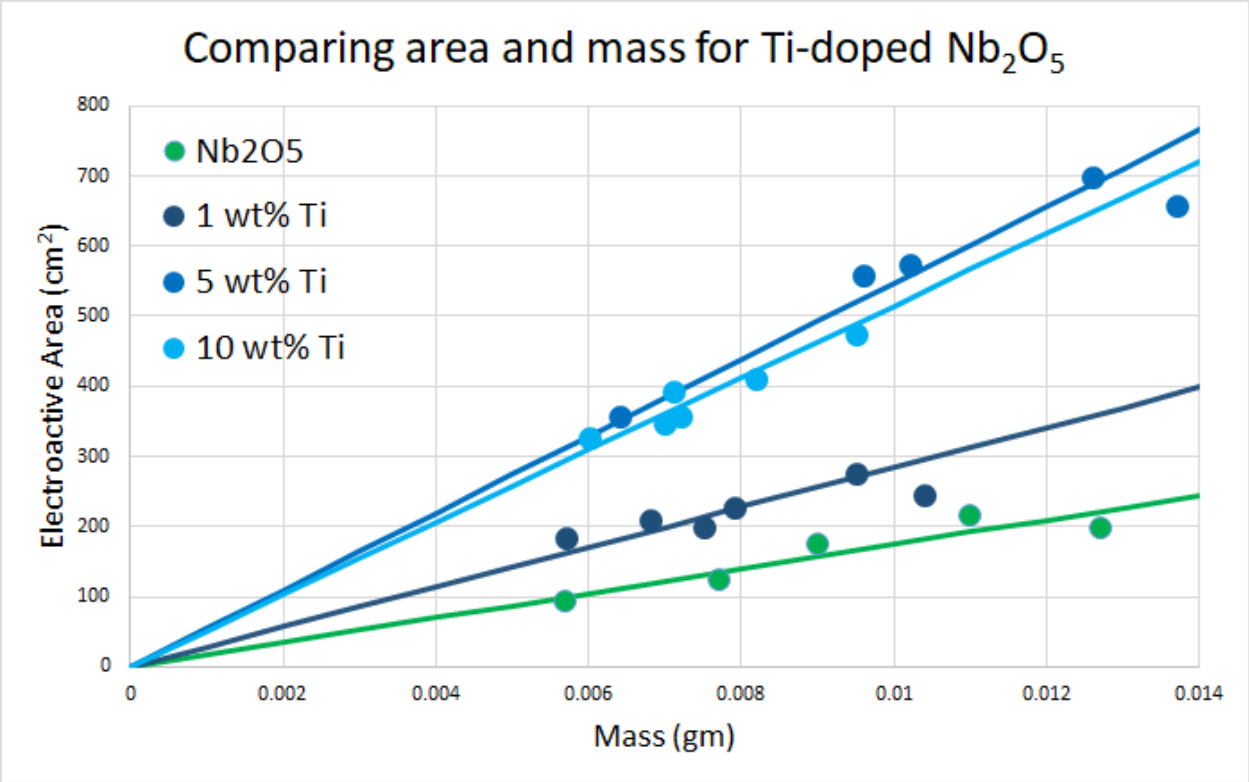

Fig. 3.21 Linear relationship between electroactive area and mass for samples of (10 w/o W and 10, 5, 1, or 0 w/o Ti)-Nb_2O_5 impregnated carbon felt

Using the same dopant levels, samples made with zirconium also showed a marked increase in electroactive area at the 5 and 10 w/o concentrations. Samples made with 1 w/o Zr

showed no noticeable difference from (10 w/o W) Nb_2O_5 samples. Similar to the case for titanium, the 5 and 10 w/o dopant concentrations for zirconium showed no difference in electroactive area, indicating a solubility limit is reached somewhere between 1 and 5 w/o Zr in Nb_2O_5.

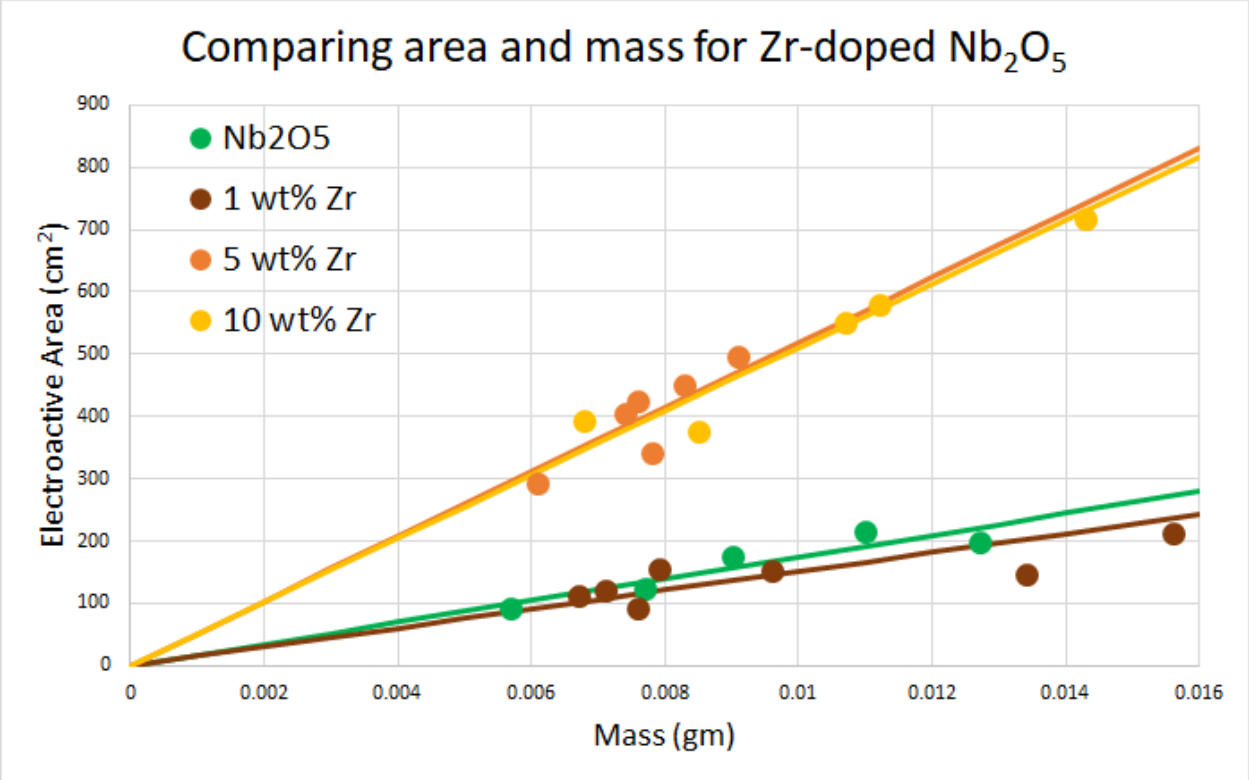

Fig. 3.22 Linear relationship between electroactive area and mass for samples of (10 w/o W and 10, 5, 1, or 0 w/o Zr)-Nb_2O_5 impregnated carbon felt

In the case of molybdenum doping, no dopant concentration showed the level of improvement seen with zirconium and titanium doping. At the levels of 1 and 5 w/o Mo, there was no measurable difference in electroactive area at all, and samples made with 10 w/o Mo showed slight improvement in electroactive area.

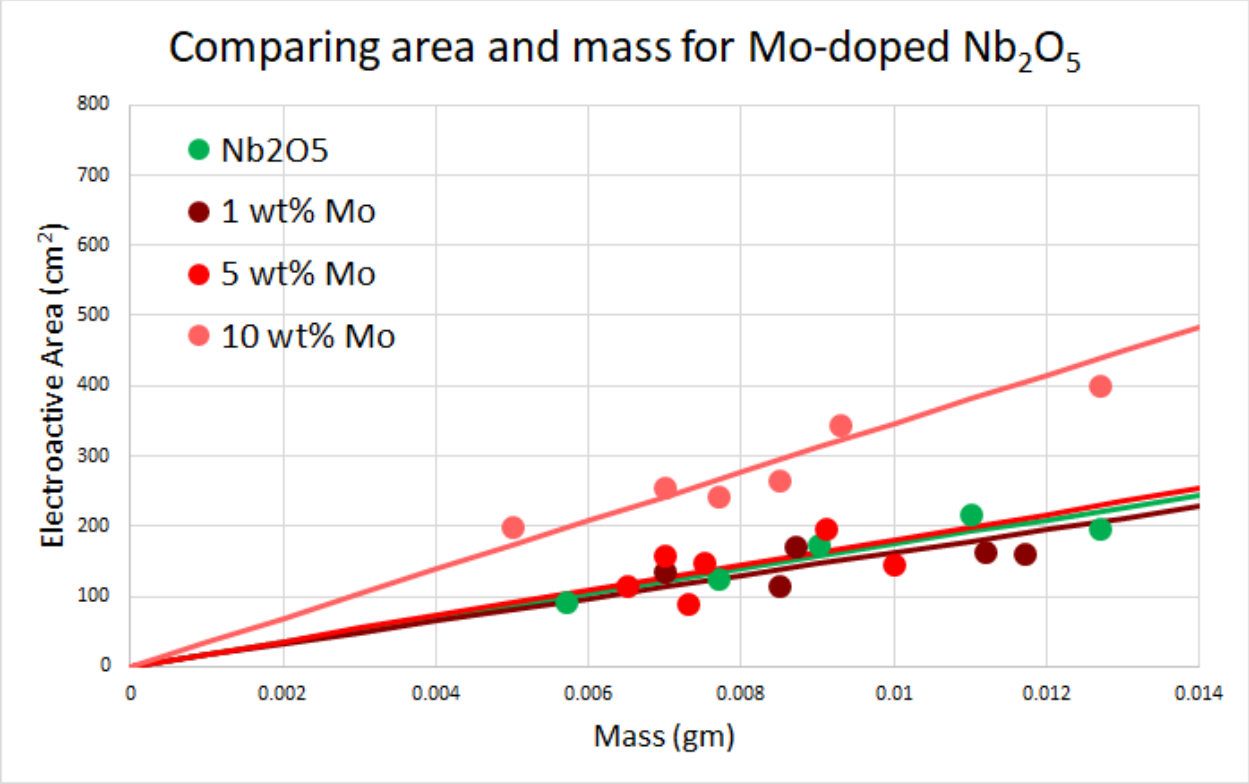

Fig. 3.23 Linear relationship between electroactive area and mass for samples of (10 w/o W and 10, 5, 1, or 0 w/o Mo)-Nb_2O_5 impregnated carbon felt

Samples were made with 10 w/o Ti, Zr, and Mo using the same niobium precursor (ammonium niobium oxalate) with the tungsten precursor absent in an effort to explore the electroactive function of the tungsten dopant. The results are shown in Fig. 3.24.

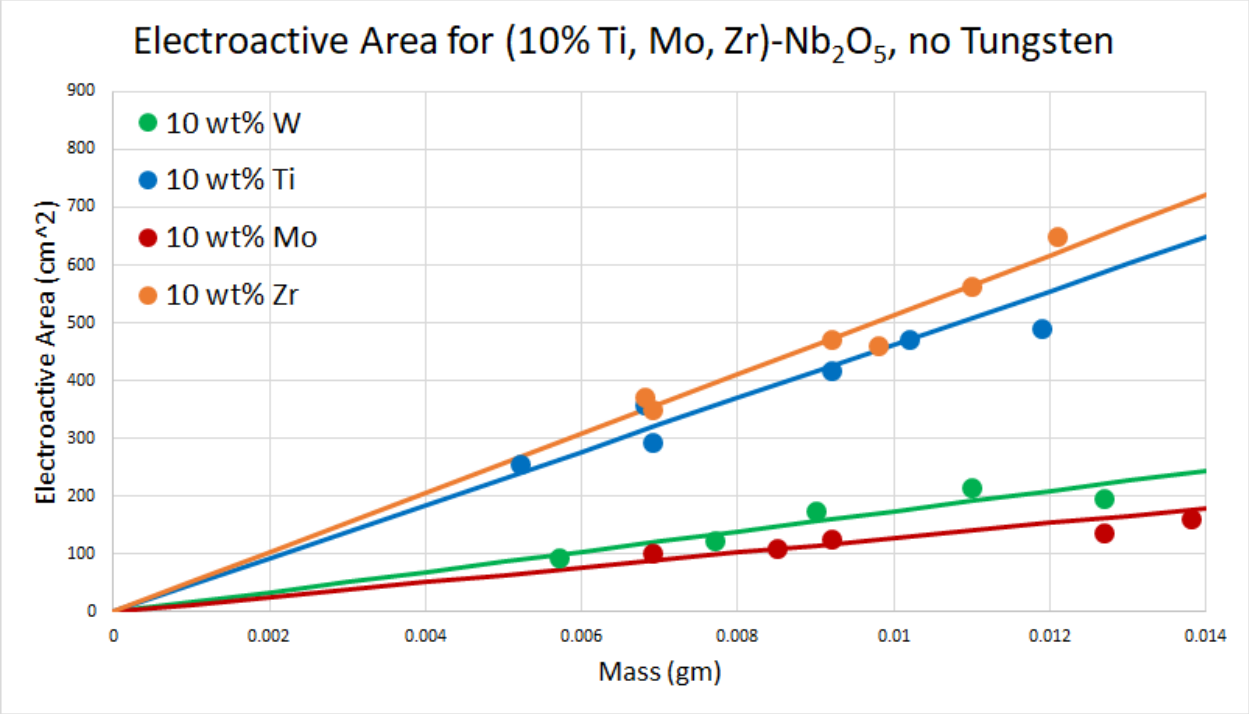

Fig. 3.24 Electroactive area plotted against sample mass for samples with 10 wt% Ti, Mo, or Zr, with no W. The data for (10 w/o W)-Nb_2O_5 are included for comparison.

The significance of the addition of tungsten seems to vary between sample compositions. For samples including titanium, there was a slight improvement when tungsten was present. Since the addition of further titanium past some point between 1 and 5 w/o had no additional effect, it is reasonable to conclude that the addition of tungsten affected the oxide structure via a different mechanism. In samples including zirconium, the presence of tungsten seems to have had no significant impact on electroactive area. For samples including molybdenum, the presence of tungsten had a slight, negative impact on electroactive area. For no dopant was the addition of tungsten found to have a large impact.

3.4 ELECTROCHEMICAL IMPEDANCE SPECTROSCOPY

All tests followed the same protocol. The signal amplitude was fixed at 5 mV relative to the open circuit voltage measured at the beginning of the test. The frequency range was 100,000 to 0.01 Hz, with ten data points collected per decade. Data fitting was done using ZView2 software. By isolating the frequency range in which each charge transfer process dominated circuit behavior, each charge transfer process could be individually measured for values of R, CPE-T, and CPE-P. The solution resistance, R_s, was found in a straightforward manner from the intersection of the EIS curve and the real axis, Re(Z). Additional fitting optimization was performed for the whole measured frequency range.

The Nyquist plots of the EIS data typically had $R_{CF} \gg R_{OX}$, and for the compositions which showed poor kinetics and low effective area, R_{CF} was so large that the shape of the plot was determined by the second charge transfer process, which totally obscured the first charge transfer process. One example is shown in Fig. 3.25. The measured data are plotted with a "partial fit" line, which omits the first charge transfer process and uses the same values of the remaining circuit parameters (except for R_S, which was manually calculated so that the two fitting curves would show greater resemblance). The high-frequency region where the measured data and the "partial fit" visibly diverge is not easily recognized as containing a second charge-transfer process, which would have the shape of a flattened semicircle on a Nyquist plot.

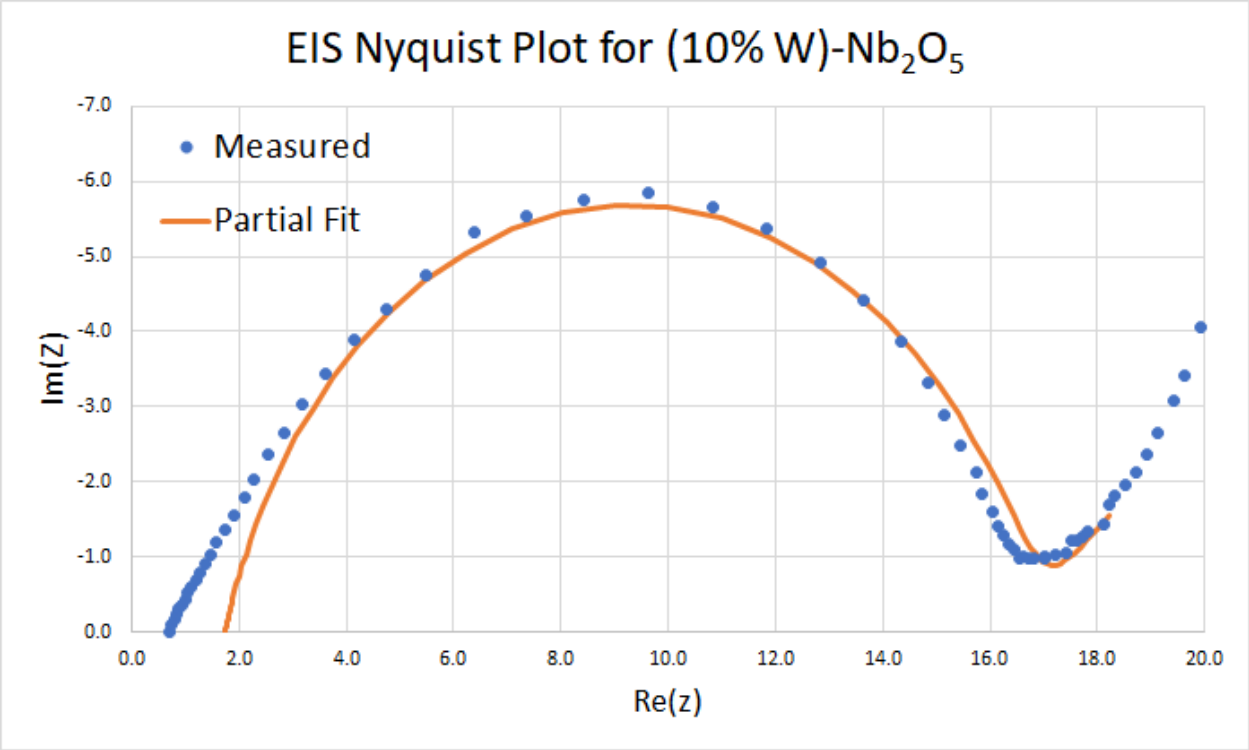

Fig. 3.25 Nyquist plot of EIS results for a sample of 0.0114 grams of carbon felt impregnated with Nb_2O_5 with 10 w/o W. As shown, kinetics are dominated by the resistance of the second charge transfer process, and the first charge transfer process is obscured.

The mathematical fitting software was used to find the best fit parameters for the first charge transfer process nonetheless, and the complete circuit was used to simulate a "full fit" curve which much better resembled the measured data.

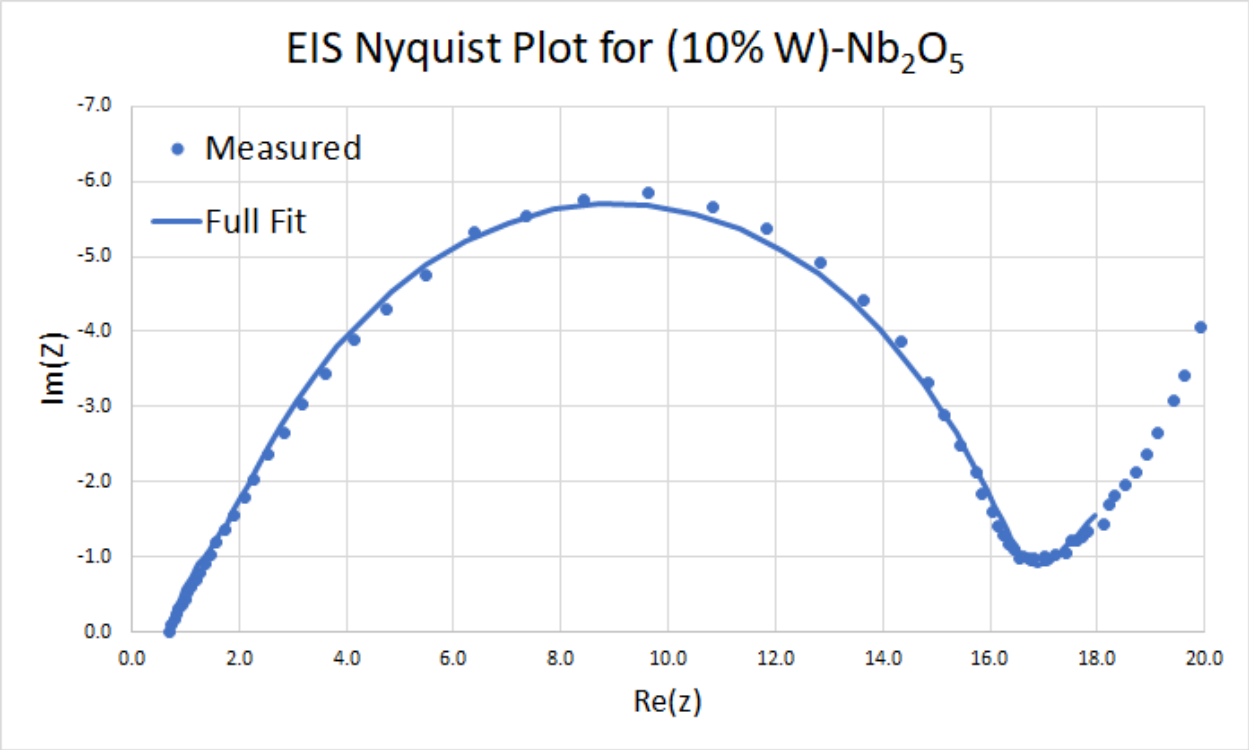

Fig. 3.26 Nyquist plot of Fig. 3.25, using modeled parameters for the full equivalent circuit of Fig. 1.3

For the compositions with higher electroactive area (5 or 10 w/o Ti or Zr), the first charge transfer process was generally distinct and showed the expected semicircular shape. In all samples, the resistance of the first charge transfer process was smaller than the second, reflected both graphically and in the fitting parameters calculated. An example is shown here.

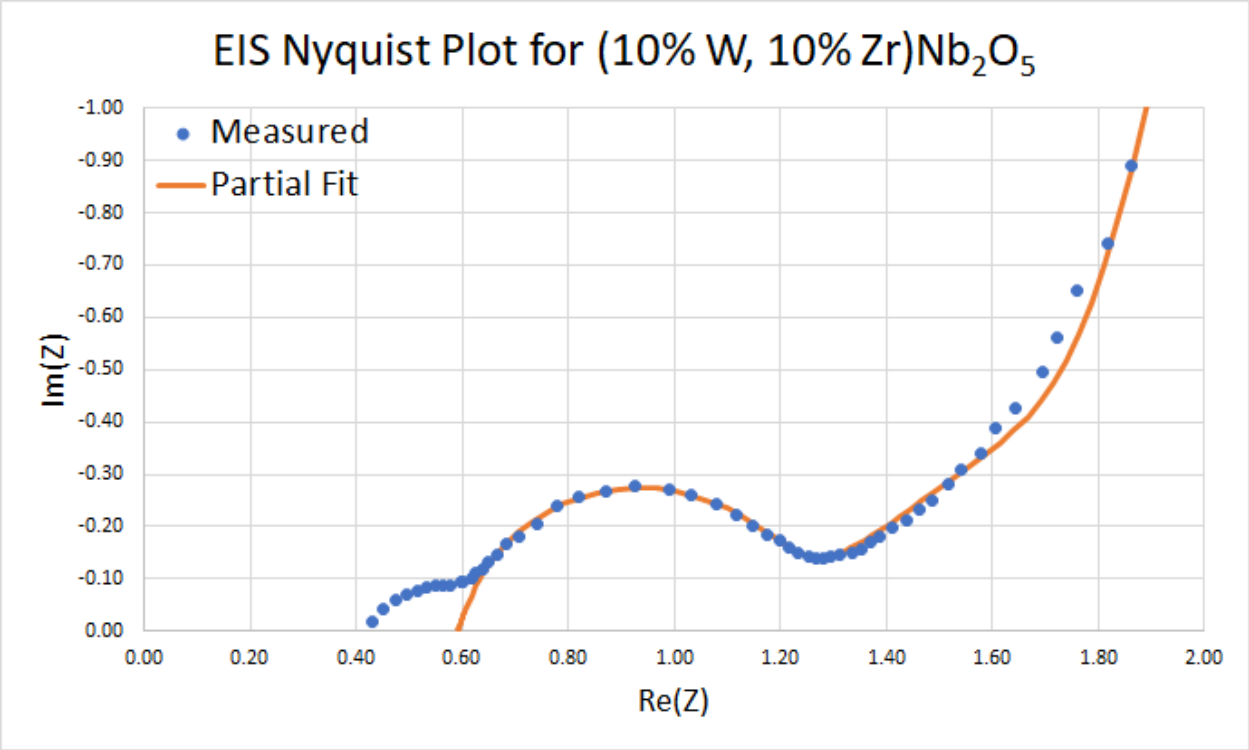

Fig. 3.27 EIS for a sample of 10 w/o Zr Nb_2O_5 showed facile kinetics and two distinct charge transfer processes. The partial fit line included used the model parameters for a single charge transfer process to highlight the emergent shape of the first charge transfer process.

A comparison of the EIS data for samples with Ti-doping showed interesting results, mostly in agreement with what would be expected from the electroactive area comparison (see Table 3.2).

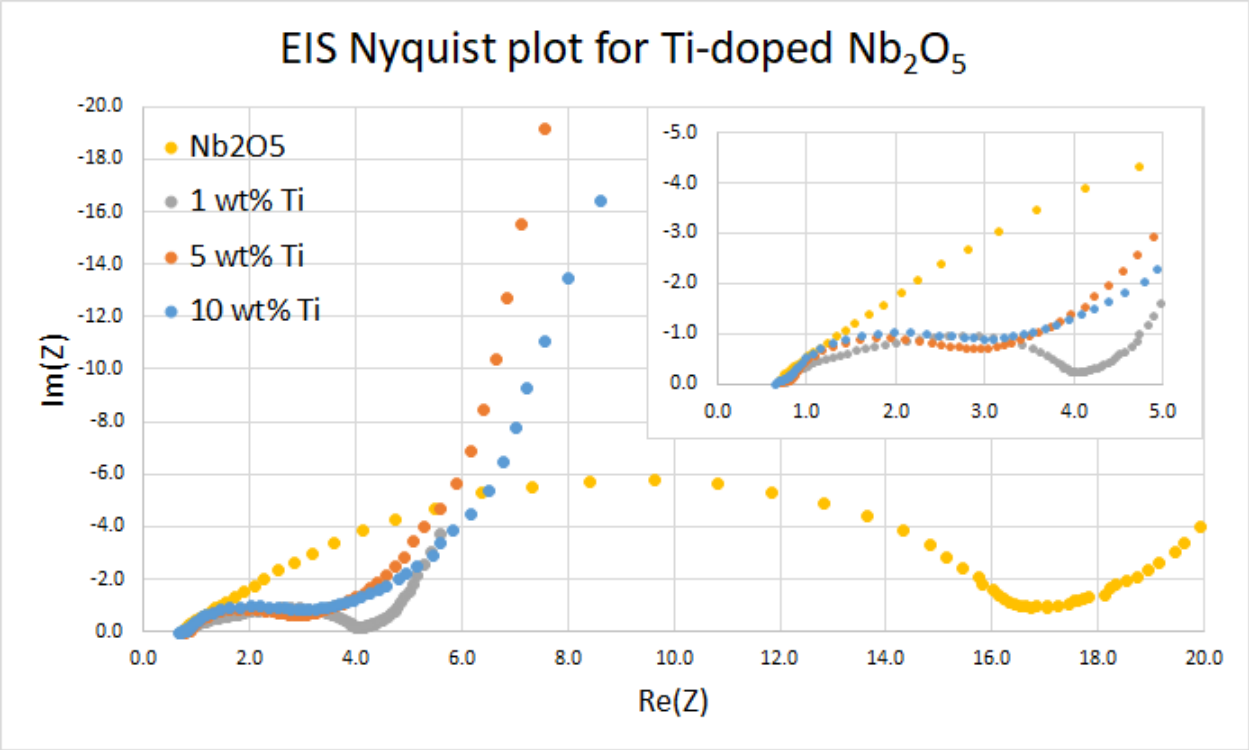

Fig. 3.28 Nyquist plots for all tested compositions with Ti-doping. The inset graph is included to highlight the high-frequency behavior and show the distinction in the first charge-transfer process resistances.

The 5 and 10 w/o Ti compositions showed greatly improved charge-transfer resistance over the (10 w/o W) Nb_2O_5 samples, as expected. The 1 w/o Ti composition showed almost the same magnitude of improvement in R_{CF}, which was not expected. The fitting parameters are summarized in Table 3.3.

Table 3.3: EIS fitting parameters for Fig. 3.28

	Solution	First Charge Transfer			Second Charge Transfer		
	R_s	**R_{OX}**	$CPET_{OX}$	$CPEP_{OX}$	**R_{CF}**	$CPET_{CF}$	$CPEP_{CF}$
Nb_2O_5	0.733	**0.736**	$1.39*10^{-4}$	0.929	**14.97**	$4.43*10^{-4}$	0.821
1 w/o Ti	0.811	**0.608**	$1.10*10^{-4}$	0.956	**2.54**	$1.29*10^{-3}$	0.792
5 w/o Ti	0.723	**0.027**	$1.39*10^{-5}$	1.41	**1.46**	$2.60*10^{-3}$	0.972
10 w/o Ti	0.651	**0.027**	$1.33*10^{-5}$	1.41	**1.53**	$2.71*10^{-3}$	0.969

It was anticipated that the values describing the first charge transfer process would be fairly constant, and that the surface morphology and functionality of the nanocrystals would be relatively unchanged by the presence, type, or level of dopants. EIS measurements seem to show that this assumption was incorrect. The values of the model parameters indicate that the 1 w/o doping level of Ti shows a significant increase in the charge transfer resistance between the oxide layer and the carbon felt, but only a modest improvement in the charge transfer resistance between the electrolyte and the surface of the oxide layer. This overall difference in resistances is consistent with the measurements of electroactive area. Further, the 5 and 10 w/o Ti samples showed very similar electroactive area, and had nearly identical fitting parameters. The differences between the two charge transfer resistances in these samples indicates that the presence of the Ti dopant both increases the conductivity of the bulk Nb_2O_5 and improves the electroactivity of the surface.

The EIS data for Mo doping also show results consistent with the electroactive area measured above, but not to the same extent. At the doping level of 1 w/o, the second charge transfer process showed much higher resistance, which manifests as the reduction in electroactive area over the (10 w/o W) Nb_2O_5 control, though the area difference is only slight

and the charge transfer resistance is much higher. The 5 w/o Mo composition had nearly the same values for charge transfer resistances. The 10 w/o Mo composition showed only a modest improvement in area, and the EIS data indicate that the higher levels of molybdenum reduce the second charge transfer process resistance but adversely changes the surface of the oxide layer, increasing the first charge transfer process resistance and also increasing the ideal capacitance (CPE-T_{OX}) by about a factor of 3 above the other compositions.

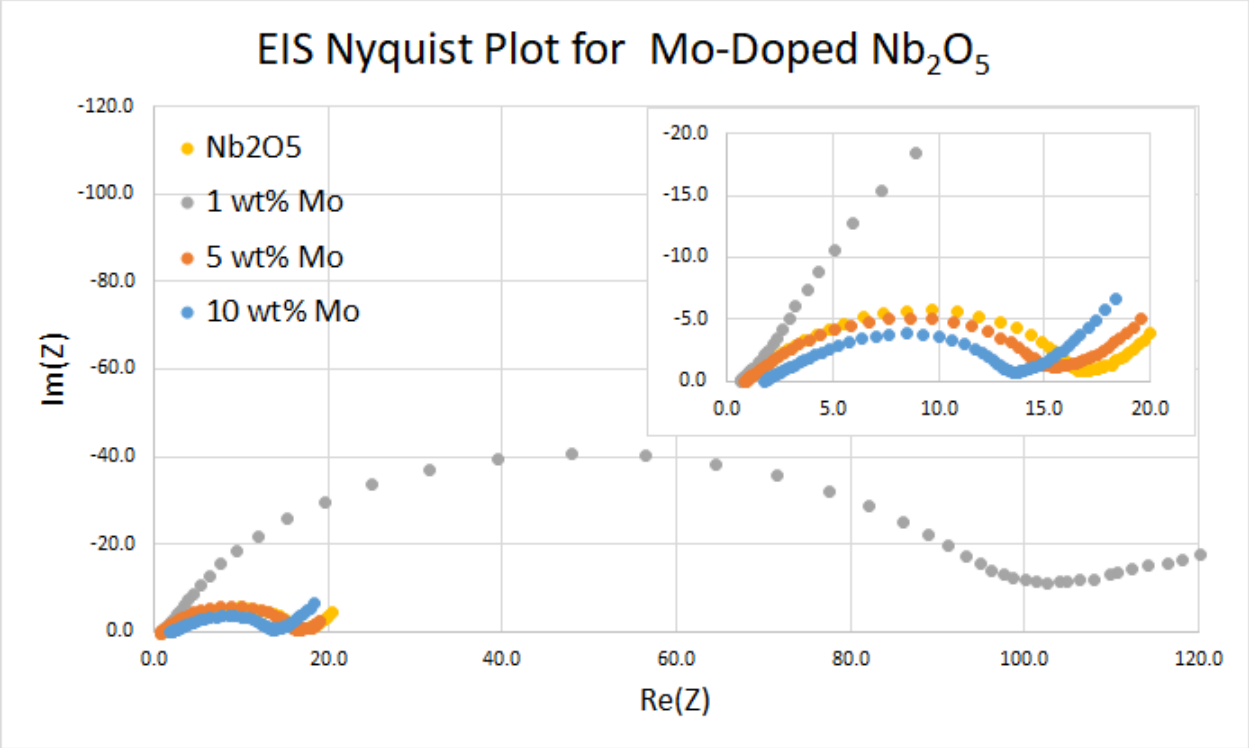

Fig. 3.29 Nyquist plots for all tested compositions with Mo-doping. The 1 w/o composition showed such high charge transfer resistance that the other three compositions are not easily differentiated on the same axes.

Table 3.4 EIS fitting parameters for Fig. 3.29

	Solution	First Charge Transfer			Second Charge Transfer		
	R_s	**R_{OX}**	$CPET_{OX}$	$CPEP_{OX}$	**R_{CF}**	$CPET_{CF}$	$CPEP_{CF}$
Nb_2O_5	0.733	**0.736**	$1.39*10^{-4}$	0.929	**14.97**	$4.43*10^{-4}$	0.821
1 w/o Mo	0.579	**0.819**	$9.73*10^{-5}$	0.949	**95.91**	$1.97*10^{-4}$	0.879
5 w/o Mo	0.527	**0.747**	$1.33*10^{-4}$	0.899	**14.49**	$2.09*10^{-4}$	0.870
10 w/o Mo	1.680	**1.731**	$3.47*10^{-4}$	0.760	**9.18**	$4.07*10^{-4}$	0.858

The extreme increase in R_{CF} for the 1 w/o Mo composition made finding a fitting value for R_{OX} very imprecise, and no conclusions should be reached from the apparent increase in the value of R_{OX} for that sample. It is likely that the true value is unchanged from the R_{OX} values for the (10 w/o W) and (10 w/o W, 5 w/o Mo) compositions. As the Mo dopant level increased, the value of R_{CF} did decrease somewhat, in keeping with the modest improvement in electroactive area, though this was somewhat offset by the increase in R_{OX}. Unlike the Ti-doped samples, the 5 w/o and 10 w/o compositions were distinct, and the addition of further molybdenum may have an increased effect on the relevant charge transfer processes.

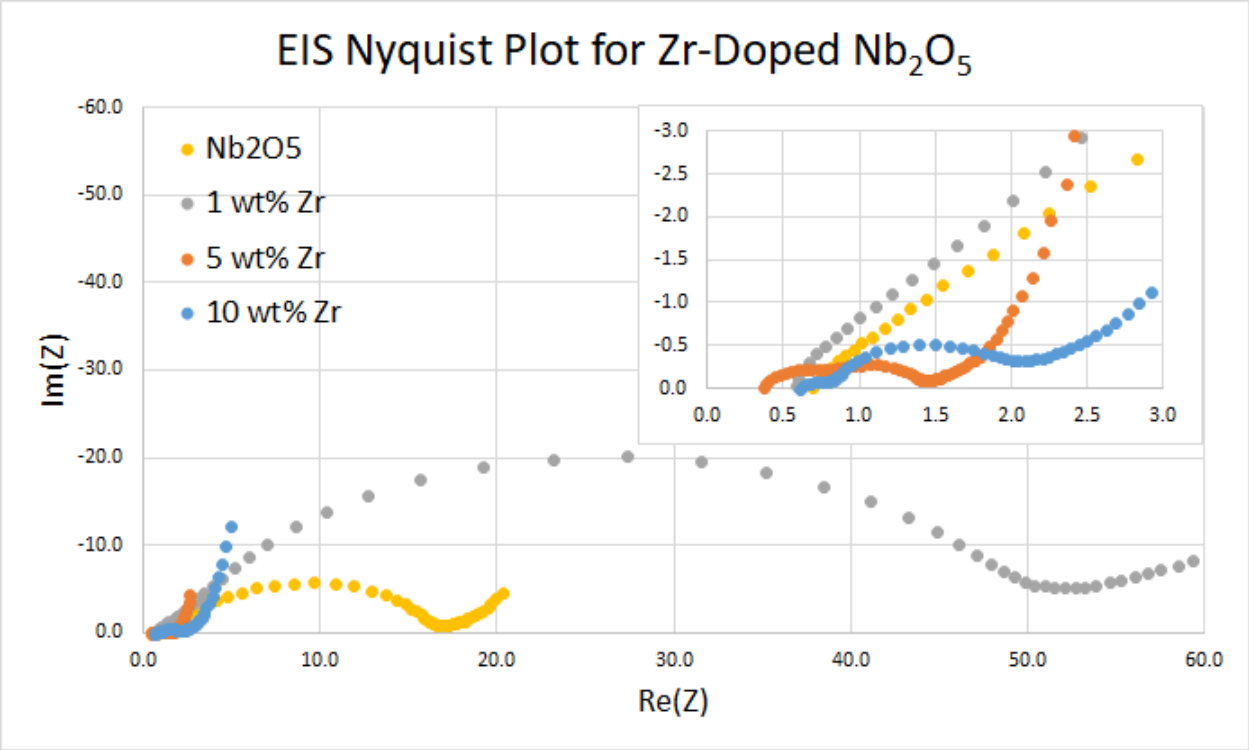

Fig. 3.30 Nyquist plots for all tested compositions with Zr-doping. Inset graph highlights the differences between the 5 and 10 w/o compositions.

The 1 w/o Zr concentration showed higher charge transfer resistance than the (10 w/o W) samples, consistent with its lower area. The 5 and 10 w/o concentrations showed much better charge transfer resistances, which is also consistent with measured effective area, though the shape of the two Nyquist plots are notably different.

Table 3.5 EIS Parameters for Fig. 3.30

	Solution	First Charge Transfer			Second Charge Transfer		
	R_s	**R_{OX}**	$CPET_{OX}$	$CPEP_{OX}$	**R_{CF}**	$CPET_{CF}$	$CPEP_{CF}$
Nb_2O_5	0.733	**0.736**	$1.39*10^{-4}$	0.929	**14.97**	$4.43*10^{-4}$	0.821
1 w/o Zr	0.593	**1.17**	$6.59*10^{-3}$	0.956	**47.67**	$2.10*10^{-4}$	0.863
5 w/o Zr	0.383	**0.429**	$1.54*10^{-4}$	0.919	**0.614**	$1.80*10^{-3}$	0.904
10 w/o Zr	0.600	**0.155**	$1.99*10^{-4}$	0.946	**0.898**	$3.02*10^{-3}$	0.954

Similar to the case for molybdenum doping, the 1 w/o level offered a significant increase in charge transfer resistance, and again, the fitting value of R_{OX} at this dopant level is imprecise. This is consistent with the decrease in electroactive area observed for this sample. It is possible that R_{OX} for zirconium doping decreases more consistently as the level of zirconium dopant is increased. The 5 and 10 w/o concentrations showed nearly identical effective areas but markedly different charge transfer resistances. The decrease in R_{OX} for the 10 w/o concentration is offset by the increase in R_{CF}, but the total linear charge transfer resistances (1.043Ω for 5 w/o and 1.053Ω) are in very close agreement. It may be a mere coincidence, then, that the 5 and 10 w/o concentrations showed the same effective area, and there may be a point of optimization between these two concentrations.

3.5 Gas Sorption Analysis

Through electrochemical means, an imprecise measurement of the actual area of the sample can be attempted using the kinetics theory outlined previously. This area is compared to the area measured by nitrogen gas sorption, calculated through DFT and BET theory. Porosity was analyzed from the same adsorption and desorption isotherms by DFT theory.

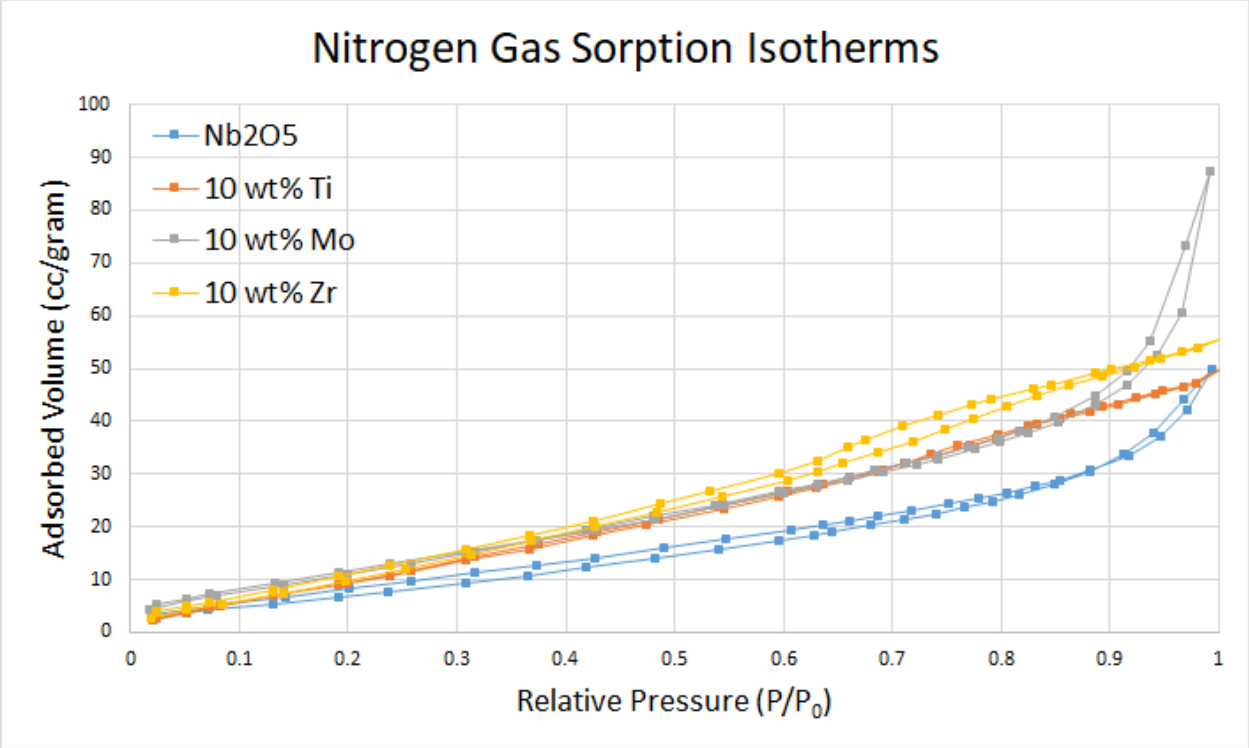

Fig. 3.31 Isothermal gas adsorption and desorption for selected samples

Table 3.6 Summary of Surface Area and Pore Characteristics for Selected Samples Shown in Fig. 3.29

Sample	DFT Area (m^2/gram)	DFT Pore Volume (cc/gram)	DFT Pore Diameter (nm)
(10 w/o W)-Nb_2O_5	18.744	0.064	3.169
(10 w/o W, Ti)-Nb_2O_5	24.412	0.068	1.410
(10 w/o W, Mo)-Nb_2O_5	29.148	0.104	2.897
(10 w/o W, Zr)-Nb_2O_5	30.946	0.078	3.169

The addition of dopants at the 10 w/o level increased the porosity at least slightly in all cases, and substantially in the case of molybdenum. The zirconium and molybdenum dopants showed no change in average pore diameter, while titanium dramatically reduced pore diameter.

These area measurements are markedly different from those found by multi-point BET analysis; see below.

From the electrochemical methods described above, the area of some samples could be estimated by the use of electrochemical parameters. For some samples (values in boldface in table 5) which showed slow kinetics, the average peak splitting was too large to be accurately converted to a value of **Λ**, and for these samples the value 0.78 was used for K.

Table 3.7 Estimated Area per Mass from Electrochemical Parameters
(Values reported as 10^2 cm^2/gram)

	Ti	Mo	Zr
10 w/o	6.06	**4.44**	5.81
5 w/o	6.59	**2.32**	5.90
1 w/o	**3.65**	**2.09**	**1.97**
(10 w/o W) Nb_2O_5	2.11		
Bare carbon felt	6.79		

These values can be compared to the geometric area measured by gas sorption and BET analysis. Without compressing the carbon felt, which would potentially modify the measurement, the most mass that could be tested was about 30 mg, which had less area than the 15 m^2 recommended for measurement by the equipment manufacturer for this instrument, and that effect introduced some error.

Table 3.8 Measured Area by Gas Sorption, Multi-Point BET Method (m^2/gram)

	Ti	Mo	Zr
10 w/o	54.145	50.282	54.286
5 w/o	51.807	67.457	50.945
1 w/o	45.545	65.623	19.795
(10 w/o W) Nb_2O_5	36.956		
Bare carbon felt	64.826		

The area of the as-delivered carbon felt was also measured, as 49.797 m^2/gram. The measurement of (10 w/o W, 1 w/o Zr)-Nb_2O_5 is highly suspect: it had a fitting error of approximately 50% and had total measured area less than 1 m^2.

By comparison with Table X, several significant effects can be noted. First, the true area measured by gas sorption is orders of magnitude higher than the electroactive area. This seems to indicate that a large portion of the carbon felt surface area is not electrochemically available, which could be due to two effects: some surface area may be in pores small enough to restrict diffusion significantly; and some fibers of the carbon felt are not electrically connected to the electrode. As mentioned previously, this latter effect was hypothesized as the cause of the apparent loss of surface area in samples of mass greater than about 15 mg but appeared to be constant below that threshold.

Second, all tested oxide compositions had the net effect of lowering the area, relative to the activated carbon felt control, indicating that the surface area inside the pores of activated carbon felt which is made inaccessible by the presence of the oxide layer is greater than the surface area added by the geometry of the oxide layer.

Third, because electroactive area and true surface area do not scale directly, the comparison can be used to estimate the electrochemical effectiveness of oxide composition independent of the effect on surface area.

The addition of titanium causes an increase in surface area which slows or stops between 1 and 5 w/o levels. The electroactive area does not increase between the 5 and 10 w/o levels, meaning that its electrocatalytic effect and its effect on conductivity are constant in this region, which is also consistent with the EIS data. However, the drop in resistance to the first charge transfer process is much greater than can be accounted for by an increase in surface area, indicating the presence of an electrocatalytic effect of titanium.

Molybdenum doping increased the actual surface area but reduced both the electroactive and electrically available areas, showing it to be electrochemically ineffective. High levels of molybdenum are not as effective at increasing the area, but are more effective electrochemically. From the EIS data, this may explain the increase in the first charge transfer resistance process, by reducing the surface area rather than changing any local electrochemical effect at the surface, while reducing the second charge transfer resistance by improving conductivity.

The addition of 1 w/o zirconium showed a significant decrease in total surface area and a similar reduction in electroactive area, without a noticeable effect on electrochemical kinetics. The further addition of zirconium markedly improved the surface area and greatly improved the electroactive area, indicating that zirconium shows electrocatalytic effectiveness and a beneficial effect on oxide deposition starting somewhere between 1 and 5 w/o. Below that level, zirconium shows no electrocatalytic effect and reduces the sample surface area.

Chapter 4. CONCLUSION

Zirconium and titanium are both viable as electrocatalytic dopants in (10 w/o W)-Nb_2O_5 impregnated carbon felt, towards the reduction of vanadium 5+ ions. This effectiveness is manifested as a change in both electrical and structural properties of the oxide layer. Molybdenum is ineffective in this role. The expected morphology, of sparsely distributed nanorod clusters, could not be achieved, and more experimentation could uncover the process of fabricating doped Nb_2O_5 of this structure, which may show a higher level of electrochemical improvement.

Further improvements to the experiment would involve better characterization of the surface properties of doped oxides to determine how the surface functionality changes due to the presence of titanium or zirconium. Additional refinements in the composition of each dopant could locate the maximum level of electrocatalysis for each dopant, but it can be speculated that the ideal zirconium composition occurs somewhere between 1 and 10 w/o, and that titanium reaches a maximum benefit somewhere between 1 and 5 w/o and the further addition of titanium above the ideal level has a diminished effect. By observing the operation of a flow cell, the impact of changing surface morphology on electrolyte hydrodynamic resistance could be quantified, as well as the coulombic efficiency and capacity retention.

BIBLIOGRAPHY

[1] M. Skyllas-Kazacos, R.G. Robbins, All vanadium redox battery, U.S. Patent No. 849,094 (1986).

[2] M. Skyllas-Kazacos, M. Rychcik, R.G. Robbins, A.G. Fane, M. Green, J. Electrochem. Soc. 113 (5) (1986) 1057.

[3] Bin Li and Jun Liu. "Progress and Directions in Low-Cost Redox Flow Batteries for Large-Scale Energy Storage." Natl Sci Rev, 2017, Vol. 4, No. 1, 91-105.

[4] Zhenguo Yang, Jianlu Zhang, Michael C. W. Kintner-Meyer, Xiaochuan Lu, Daiwon Choi, John P. Lemmon, and Jun Liu. "Electrochemical Energy Storage for a Green Grid." Chem. Rev. 2011, 111, 3577–3613.

[5] Chanyong Choi, Soohyun Kim, Riyul Kim, Yunsuk Choi, Soowhan Kim, Ho-young Jung, Jung Hoon Yang, and Hee-Tak Kim. "A Review of Vanadium Electrolytes for Vanadium Redox Flow Batteries." Renewable and Sustainable Energy Reviews 69 (2017) 263–274.

[6] Brian Huskinson, Michael P. Marshak, Changwon Suh, Süleyman Er, Michael R. Gerhardt, Cooper J. Galvin, Xudong Chen, Alán Aspuru-Guzik, Roy G. Gordon, and Michael J. Aziz. 2014 "A metal-free organic–inorganic aqueous flow battery." Nature 505(7482): 195-198.

[7] C. N. Schmidt and G. Cao. "Properties of Mesoporous Carbon Modified Carbon Felt for Anode of All-Vanadium Redox Flow Battery." Sci China Mater 2016, 59 (12) 1037–1050.

[8] J. Liu, Z. A. Wang, X. W. Wu, X. H. Yuan, J. P. Hu, Q. M. Zhou, Z. H. Liu, and Y. P. Wu. "Porous Carbon Derived from Disposable Shaddock Peel as an Excellent Catalyst Toward VO^{2+}/VO_2^{+} Couple for Vanadium Redox Battery." Journal of Power Sources 299 (2015) 301-308.

[9] Yuqing Huang, Qi Deng, Xiongwei Wu, and Shuangyin Wang. "N, O Co-Doped Carbon Felt for High-Performance All-Vanadium Redox Flow Battery." International Journal of Hydrogen Energy 42 (2017) 7177-7185.

[10] Bin Li, Meng Gu, Zimin Nie, Yuyan Shao, Qingtao Luo, Xiaoliang Wei, Xiaolin Li, Jie Xiao, Chongmin Wang, Vincent Sprenkle, and Wei Want. "Bismuth Nanoparticle Decorating Graphite Felt as a High-Performance Electrode for an All-Vanadium Redox Flow Battery." Nano Letters 13 (2013) 1330-1335.

[11] L. Wei, T. S. Zhou, L. Zeng, X. L. Zhou, and Y. K. Zeng. "Copper Nanoparticle-Deposited Graphite Felt Electrodes for All Vanadium Redox Flow Batteries." Applied Energy 180 (2016) 286-391.

[12] B. Li, M. Gu, Z. Nie, X. Wei, C. Wang, V. Sprenkle, and W. Wang. "Nanorod Niobium Oxide as Powerful Catalysts for an All Vanadium Redox Flow Battery." Nano Lett. 2014, 14, 158-165.

[13] Jerry Yu, Liu Yuan, Hao Wen, Mahnaz Shafiei, Matthew Richard Field, Jia Liang, Jin Yang, Zhi Fu Liu, Wojtek Wlodarski, Nunzio Motta, Yong Xiang Li, Gengmin Zhang, Kourosh Kalantar-zadeh, and Peter To Lai. "Hydrothermally formed functional niobium oxide doped tungsten nanorods." Nanotechnology 24 (2013) 495501-495513.

[14] Schäfer, H., Gruehn, R., Schulte, F. "Die Modifikationen des Niobpentoxids." Angew. Chem. 78, (1966) 28-41.

[15] Bard, Allen J., and Larry R. Faulkner. *Electrochemical Methods and Applications*. Wiley-Interscience, 2000.

[16] T. Yamamura, M. Watanabe, T. Yano, Y. Shiokawa, "Electron-Transfer Kinetics of Np3+/Np4+, NpO2+/NpO2 2+, V2+/V3+, and VO2+/VO2+ at Carbon Electrodes." J. Electrochem. Soc. 152 (2005) A830.

[17] H. Matsuda and Y. Ayabe. "Zur Theorie Der Randles-Sevcikschen Kathodenstrahl-Polarographie." Z. Elektrochem. 59 (1955) 494.

[18] S. R. Nicholson. "Theory and Application of Cyclic Voltammetry for Measurement of Electrode Reaction Kinetics." J. Anal. Chem. 37 (11) (1965) 1351-1355.

[19] Newman J, Thomas-Alyea KE. *Electrochemical Systems*. Hoboken: John Wiley & Sons; 2012.

[20] Orazem, Mark E., and Bernard Tribollet. *Electrochemical Impedance Spectroscopy*. John Wiley and Sons, Inc., 2008.

[21] Howe, J., Rawn, C., Jones, L., Ow, H., Powder Diffr., v18 p 159 (2003).

[22] Waring et al., J. Res. Natl. Bur. Stand., Sect. A, V.77 p705 (1973).